



Surface microenvironment engineering of black V_2O_5 nanostructures for visible light photodegradation of methylene blue



Ahmed Badreldin^{a,b}, Muhammad Danyal Imam^a, Yiming Wubulikasimu^a, Khaled Elsaid^a, Aya E. Abusrafa^a, Perla B. Balbuena^b, Ahmed Abdel-Wahab^{a,*}

^a Chemical Engineering Program, Texas A&M University at Qatar, P.O. Box 23874, Doha, Qatar

^b Artie McFerrin Department of Chemical Engineering, Texas A&M University, College Station, TX 77843-3122, USA

ARTICLE INFO

Article history:

Received 16 January 2021

Received in revised form 6 March 2021

Accepted 21 March 2021

Available online 23 March 2021

Keywords:

Vanadium pentoxide

Photocatalysis

Visible light photodegradation

Methylene blue

Oxygen vacancy

ABSTRACT

Utilization of photocatalysis as a promising strategy for environmental and energy applications has been widely considered. Herein, we report a novel black V_2O_5 material (bV_2O_5) synthesized using a controllable and environmentally benign physicochemical reduction method. HRTEM, ESEM, EDX, Raman, XPS, XRD, and BET textural characterization, as well as computational density functional theory (DFT) techniques were employed to understand the chemical and electronic changes obtained through modulation of the surface microenvironment. DFT analyses reveal that tuning a high degree of surface oxygen vacancies considerably ameliorated visible light photoactivity of practically inactive pristine V_2O_5 . The optimized bV_2O_5 sample yielded 92% photodegradation of 20 mg/L cationic methylene blue (MB) in 60 min under visible light irradiation – corresponding to a 58-fold increase in photodegradation efficiency over pristine V_2O_5 . Neutral quinoline yellow (QY) and anionic methyl orange (MO) photodegradation were also investigated to examine the photocatalytic efficacy of bV_2O_5 for degradation of other organic contaminants with different charges. DFT calculations show a clear thermodynamic stability towards reduction of the predominant polar (001) facet at 1-coordinated oxygen surface site. A staggered (type-II) heterostructure between pristine and reduced V_2O_5 was determined from band edge positions which is believed to promote the enhancement in photoactivity of the reduced sample by offering favorable electron-hole separation and allowing both hydroxyl and superoxide radical formation. The mechanism behind the formation of surface defects on bV_2O_5 was proposed based on configurational changes.

© 2021 The Author(s). Published by Elsevier B.V.
CC-BY_4.0

1. Introduction

Over two billion people worldwide lack ample and effective access to safe potable water [1]. Bench-scale treatment facilities that are easy to operate and maintain in remote locations can find wide implementation in curbing the impact of potable water availability. An array of water pollutants, including but not limited to, heavy metals (i.e., Hg^{2+}), persistent pharmaceutical antibiotics, and organic dyes have been deemed problematic in different water bodies consequential towards many ecosystems affecting humans [2,3]. Organic compounds have been found to be some of the most omnipresent and persistent contaminants found in land wastewaters [4]. As such, benign environmental remediation of contaminated waters containing textile azo dyes and other organic contaminants

has been an area of significant research. Efficient and cost-effective photodegradation of these contaminants relies on catalysts with high activity in the visible-light region, favorable kinetics, and resilient performance stability. The development of black TiO_2 led to an unprecedented growth of interest due to significant improvements in photoactivity and kinetics. However, a lack of attention has been given towards investigating the photoactivity of other transition metal oxides (TMO) upon chemical reduction. Several technologies that can be implemented for removal of organic contaminants from wastewater include heterogenous photodegradation [5,6], bioremediation [7], ozonation [8], adsorption [9], and Fenton [10] processes have been proposed and heavily investigated. Among these techniques, photocatalytic degradation has seen a growing interest as it can be operated with cost-effective and abundant semiconductor materials that are capable to degrade contaminants in-situ.

Briefly, conventional photocatalytic processes involve a reaction that is activated by absorption of a photon with sufficient energy to

* Corresponding author.

E-mail address: ahmed.wahab@qatar.tamu.edu (A. Abdel-Wahab).

overcome the bandgap energy of the photoactive material used – whereby the reaction occurs at the photocatalyst-water interface. Photocatalytic materials have been investigated, optimized and employed in an array of applications including water treatment [11], antimicrobial coatings [12], and water splitting [13]. Upon photo-excitation, the electron (e^-) energizing to the conduction band (CB) generates an oxidizing radical (O_2^{\bullet}), and the resultant hole (h^+) at the valence band (VB) either oxidizes an organic contaminant or reacts with available water molecules resulting in hydroxide radical ($\bullet OH$) which can easily oxidize organic contaminants. Thus, it is during the intermittent time that the electron is at the CB that photodegradation of a contaminant is feasible due to the near-simultaneous generation of oxidizing radicals. In the scenario that the recombination rate exceeds the time it takes to generate an oxidizing radical, the photoexcitation process is essentially wasted, subsequently decreasing the apparent photoactivity and quantum efficiency of the photocatalyst. Accepted approaches that have been implemented and confirmed in previous works towards specifically decreasing the electron-hole recombination rate include doping and carbon-based heterojunctions which consistently yield a corresponding enhancement in performance of base photocatalyst [14–16]. Several reports have identified that a catalyst loading of 0.5 g/L is optimum for allowing the highest degree of reactive species formation atop the photocatalyst [17]. Since photodegradation is a (*near*) surface phenomena, the formation of a hydration film around the photocatalyst hampers the organic molecules from adsorbing – a fundamental step of any photochemical process [18]. Thus, the favorable modulation of the semiconductor's micro-environment interface enhances the elementary surface adsorption step, such that an inherent improvement in the apparent kinetics of the photodegradation is facilitated.

Photocatalysis research has seen growing interest after the discovery of 'black' TiO_2 by Chen and coworkers [19] in 2011, which showed superior photoactivity performance under visible light irradiation compared to its pristine counterpart. The reason behind that enhancement has been predominantly attributed to high density of band tail states caused by excessive disorder, which reduce the effective bandgap of the material and creates *trap states* during electron-hole recombination. A considerable fraction of the sun's energy is in the visible (43%) and infrared (52%) region, with a very small segment in the UV (5%). A myriad of metal oxide photocatalysts including TiO_2 [20–22], ZnO [23–25], WO_3 [26], and V_2O_5 [27] have a very poor spectral response outside the UV region [28–31]. This inhibits their potential of harvesting a higher degree of photons to partake in a successful photochemical reaction. Metal-doping on metal oxides tends to improve the spectral response but this significantly affects the crystallinity of the material due to the consequential formation of secondary impurities, which reduce efficiency and photoactivity [32,33]. Non-metal doping techniques were found to enhance the spectral response in the visible range while maintaining the initial crystallinity of the material [34,35]. Nonetheless, improvement in photoactivity seems to still be limited due to inadvertent effects that may occur such as the decrease of initial crystallite size. This directly limits photoactivity since it decreases the migration distance of a photoexcited electron – essentially increasing the electron-hole recombination rate. Intrinsic electronic modulation – such as that applied on black TiO_2 – remains quintessential to the overall observed photochemical performance and to the rapid manufacturing of photocatalysts without additional materials.

A myriad of work has been undertaken to investigate, understand, and realize the intrinsic potential enhancements caused by oxygen deficiencies in the growing field of electrocatalysis [36–39]. For instance, in our recent work, we have confirmed enhanced electrochemical activities and chemical stabilities of TMOs towards the hydrogen evolution reaction (HER) [40]. Worthy of note, there

are several intrinsic disadvantages of pristine TiO_2 towards photocatalysis, namely a large bandgap, sole UV-light response, high electron-hole recombination, amongst others relative to other TMOs with intrinsic low bandgaps, photostability, and visible-light response [41]. Controlled O_v modulation studies on bulk and surface TiO_2 found that surface Ti^{3+} species adjacent to oxygen vacant sites can act as hole scavengers, and O_v sites act as O_2 binding sites and electron scavengers. This suppresses the electron-hole recombination rate which directly enhances photoactivity [42]. Moreover, experimentally induced concentrations of partially reduced metal states (i.e. Ti^{3+}) form sublevel band states below the CB, which reduce the apparent bandgap of the overall photocatalyst. It is an interesting endeavor to study the effect of modulated O_v sites populating different TMOs which may be more appropriate for emerging persistent contaminant degradation and/or offer a refined understanding of unknown effects anionic vacancies may have on photocatalysts.

To this end, some metal oxide photocatalysts such as V_2O_5 exhibited poor photoactivity due to a deep conduction band (CB) edge limiting major reduction reactions (i.e., reduction of oxygen to superoxide radicals) from forming which can be paramount to photodegradation abilities. Therefore, implementation of V_2O_5 has been limited to its utilization in forming hetero-nanostructures with other photocatalysts [43–47]. Low cost, chemical and photostability, small bandgap, high oxygen density, high oxidation state of the transition metal involved (i.e. V^{5+}), and non-toxicity of V_2O_5 promote it as a promising candidate when considering the potential photoactivity enhancements that would occur by the creation of intrinsic oxygen vacancies (O_v). Coupling of V_2O_5 to reduced graphene oxide (RGO) was investigated and surface V^{5+} states were found to enhance e^-/h^+ separation [48]. However, photoactivity was still hampered due to the innately fast e^-/h^+ recombination rate of V_2O_5 .

In this work, a facile and environmentally benign 2-step synthesis scheme was used to fabricate V_2O_5 with high surface O_v in large batches, which interestingly results in a dark colored bV_2O_5 material. To the best of our knowledge, this is the first study to intentionally and successfully synthesize sizeable and stable V_2O_5 with a high O_v surface density. This widely adoptable technique of physicochemical and solution-based reduction using $NaBH_4$ has been used in achieving oxygen deficiencies in TiO_2 previously [49,50]. Thus, capitalizing on previous work, we innovatively appropriated this method after fine tuning $NaBH_4$ amounts and reduction temperatures, to achieve photoactive oxygen deficient V_2O_5 which exhibited novel properties of ultra-high adsorption and photodegradation relative to its pristine counterpart and other TMOs. Intrinsic properties of the novel bV_2O_5 were studied using various relevant characterization techniques. The influence of surface O_v , crystallite size, oxidation states of Vanadium, and surface charge on the photoactivity and stability of V_2O_5 were investigated using methylene blue (MB) as a model contaminant in photodegradation batch experiments under visible light. Further, DFT was employed to probe the stability, band-structure, and T/PDOS of bV_2O_5 under different O_v locations for the (001) and (110) exposed facets of the oxyanion of Vanadium. The rate of MB photodegradation using bV_2O_5 was observed to be a 58-fold higher than that of pristine V_2O_5 material. The below findings open the door to innumerable possibilities for the potential use of bV_2O_5 in photo- and electrochemical environmental and energy applications.

2. Experimental

2.1. Synthesis of reduced 'black' V_2O_5

All precursors used for material synthesis were purchased from Sigma-Aldrich and used as received without any further purification. 2.5 g of ammonium metavanadate (NH_4VO_3) was measured in an

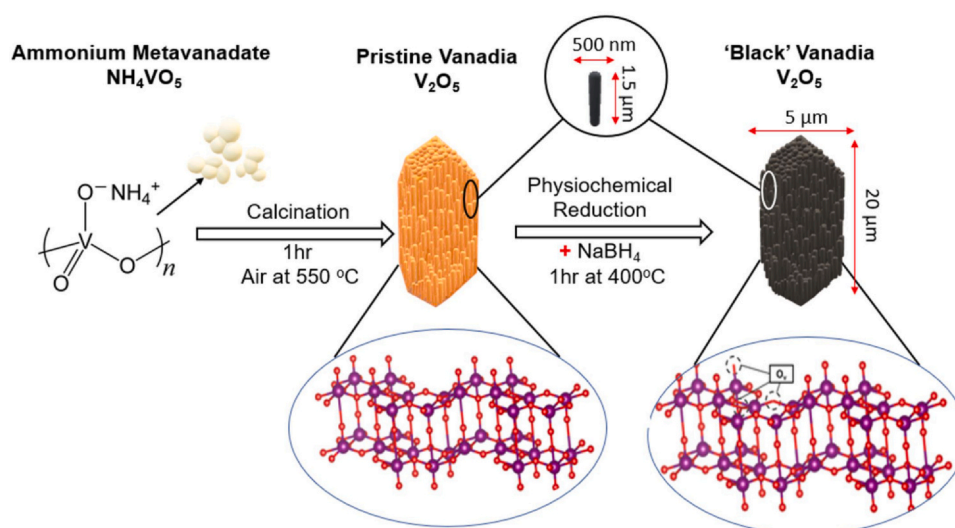


Fig. 1. Synthesis scheme employed to obtain bV₂O₅ microstructures composed of uniaxial nanorods.

alumina crucible and calcinated in a muffle furnace at 550 °C for 1 h in an air atmosphere, with a 40 °C/min heating rate from an initial temperature of 25 °C. The resulting orange-colored sample was characterized and identified as pristine V₂O₅. 1 g of the prepared pristine V₂O₅ was weighted and thoroughly mixed with 0.22 g of sodium borohydride (molar ratio of NaBH₄ to V₂O₅ at 1.05:1), and reduced in a tubular furnace at 400 °C in an argon atmosphere, with a 1 h heating time (6.25 °C/min) and 1 h reaction holding time at 400 °C. The inert argon atmosphere was appropriated in order to maintain vacant oxygen positions upon their formation through borohydride-aided reduction. The resulting sample was washed and centrifuged three times with de-ionized water, then it was vacuum-dried at a pressure of −0.1 mbarg and 75 °C for 7 h. Fig. 1 depicts the experimental scheme used with the observed textural properties from sample characterization.

2.2. Chemical, textural, and optical properties of modified V₂O₅ samples

An AXIS Ultra DLD X-ray Photoelectron Spectroscopy (XPS) was applied to collect large area survey and high-resolution X-ray Photoelectron spectra of pristine and black vanadium oxide samples. The XPS Al mono (K-alpha) radiation (1486.6 eV) source was operated at 15 kV and 15 mA emission current. The high-resolution spectra of Vanadium 2p and Oxygen 1s peaks were collected with pass energy of 20 eV and 0.1 eV step size. An integrated Kratos Vision data processing software was used for calibration of spectra, peak analysis and deconvolution.

The morphologies of the samples were analyzed utilizing high resolution scanning electron microscope (ESEM) images employing a FEI Quanta 400 environmental scanning electron microscope (FEI, Oregon, USA). The ESEM was operated at high vacuum mode with 30 Kv acceleration voltage and working distance of around 6.5 mm. An EDAX Octane Elect EDS System with silicon drift detector was used for EDS signal collection and analysis. The high-resolution transmission electron microscope (HRTEM) images were taken by an FEI Talos F200 with 200 kV acceleration voltage. HRTEM samples were prepared by first ultrasonication in ethanol, followed by drop-casting the dispersion onto TEM Cu grid (400 mesh) with holey film for characterization. Surface area and pore size distributions were analyzed using N₂ physisorption under Brunauer-Emmett-Teller (BET) and Barret-Joyner-Halenda (BJH) methods under relative pressure (P/P₀) of 0.995 at −195.8 °C with 10 s of equilibration intervals.

Crystallinity of pristine and black vanadium oxide materials were analyzed using powder XRD spectra collected via a Rigaku Ultima IV Multipurpose X-ray Diffractometer (Rigaku Corp., Tokyo, Japan) equipped with cross beam optics, fixed monochromator and a scintillation counter. The XRD radiation source (Cu-Kα) was operated at 40 kV and 40 mA. A divergence slit (2/3°), divH.L. Slit (10 mm), scattering slit (2/3°), and a receiving slit (0.3 mm) were used. The XRD data were collected using continuous scan mode in the 2θ range of 5–80° with step width of 0.02° and 1°/minute scan speed. Integrated Rigaku PDXL2 software with PDF4 + 2019 database was used for data treatment and phase analysis. Scherrer and Williamson-Hall methods were both used to approximate the average crystallite sizes of the as-prepared materials [51,52]. Raman spectroscopy was taken using a Thermo Fisher Scientific DXR Raman Microscopy, with an excitation wavelength of 532 nm at a focused scan range of 40–1250 cm^{−1}, 50-times microscope objective, 1.3 μm laser spot, and using incident laser power of 5 mW. UV-Vis-NIR diffuse reflectance spectroscopy (DRS) (PerkinElmer Lambda 950 Spectrophotometer) was used in the range of 200–800 nm to quantify the solid-state absorption of vanadium oxides. The Tauc plots were applied to obtain the bandgaps of the as-prepared V₂O₅ based photocatalysts.

2.3. DFT calculations

Spin-polarized DFT calculations were carried out within the general gradient approximation (GGA) [53] using the Perdew-Burke-Ernzerhof (PBE) [54] functional and exchange correlation (XC) functions as implemented in the Vienna ab initio simulation package (VASP) [55]. The electron-ion interactions were treated with the projected-augmented wave (PAW) functions [56]. For overcoming limitations of the PBE method in approximating bandgap and electronic properties, a Hubbard-U correction parameter was introduced [57]. The U parameter is effectively an orbital-dependent term referred to as an on-site Coulomb repulsion energy which is imported into the XC term of GGA (PBE), and follows the below relation:

$$E_{GGA+U}[n(r)] = E_{GGA}[n(r)] + E_U[n(r)] - E_{dc} \quad (1)$$

Herein, $n(r)$ is the electron density, E_{GGA} is the energy obtained from the GGA (PBE) functional calculations, E_U is the Hubbard type energy contribution, and E_{dc} is the double-counting correction energy. The Kohn-Sham orbitals were expanded using a plane-wave basis set and the kinetic cutoff energy was fixed at 500 eV. Structural convergence criteria were assumed when the Hellmann-Feynman

forces and energies were less than $0.005 \text{ eV } \text{\AA}^{-1}$ and 10^{-6} eV per atom, respectively. Gaussian smearing [58] with a finite temperature width of 0.1 eV was used to enhance convergence of state near the system-dependent Fermi levels. The Brillouin zone (BZ) was sampled using a $2 \times 4 \times 3$ k -point mesh generated by Monkhorst-Pack (MP) scheme [59] for the bulk system. For facet-dependent studies, $2 \times 2 \times 1$ supercells were constructed in the appropriate orientation, and an adequately large 15 \AA vacuum region was introduced to eliminate unphysical interactions. A $5 \times 3 \times 1$ k -point mesh for (110) faceted systems, and a $3 \times 7 \times 3$ k -point mesh for polar (001) faceted systems. Bulk pristine V_2O_5 is an orthorhombic crystal lattice, and lattice constants are $a = 11.527 \text{ \AA}$, $b = 3.614 \text{ \AA}$, and $c = 4.614 \text{ \AA}$, which are in good agreement with experimentally determined values ($a = 11.516 \text{ \AA}$, $b = 3.565 \text{ \AA}$, and $c = 4.373 \text{ \AA}$) obtained through XRD refinement of phases. Oxygen vacancy formation energies were obtained for each facet (i.e. (110), (001)) based on the following relation:

$$E_{\text{form}} = E_{p,x} - E_{b,x} + 0.5 \cdot E_{\text{O}_2} \quad (2)$$

E_{form} represents the formation energy per oxygen vacancy (O_v) site, $E_{p,x}$ is the total energy of the pristine system, $E_{b,x}$ is the total energy of the reduced/oxygen vacant system, and E_{O_2} is the energy of diatomic oxygen obtained from a $10 \times 10 \times 10$ supercell with a $1 \times 1 \times 1$ k -point mesh. p , b , and x represent pristine, black/reduced, and exposed facet, respectively.

2.4. Determination of total organic contaminant adsorptive capacity

Before the analysis of photoactivity, the total organic contaminant adsorptive capacity of each sample was assessed using methylene blue (MB) as the contaminant dye. Throughout all adsorption and photodegradation experiments, the pH of the solution was adjusted to pH 7.0 by adding HCl or KOH solutions. Two separate 50 mL solutions of 100 mg/L MB were prepared, with 0.025 g of the pristine V_2O_5 sample added to one beaker, and the same amount of bV_2O_5 added to the second – ensuring catalyst loading is maintained at 0.5 g/L . Each sample was tip-sonicated for 1 min before the solutions were left under magnetic stirring for 3 h in the dark. A 3 mL aliquot from each solution was taken after 3 h, and UV–Vis spectroscopy was used to determine the remaining concentration of MB in each solution after adsorption equilibrium was achieved and the adsorption capacity was calculated as follow,

$$\text{Adsorption Capacity} = C_0 - C_{3\text{hrs}},$$

where, C_0 is the initial concentration of organic dye (100 mg/L) and $C_{3\text{hrs}}$ is the concentration of dye in mg/L after 3 h of dark adsorption. The total MB adsorptive capacity for the pristine and bV_2O_5 samples was found to be approximately 25 mg/L and 75 mg/L , respectively.

2.5. Photodegradation experiment

Photoactivity of both pristine and bV_2O_5 samples was evaluated using methylene blue (MB) as the target organic contaminant. Catalyst load was maintained at 0.5 g/L for all kinetic experiments and the stock solutions of MB were prepared as such to ensure 20 mg/L of MB remained in solution after adsorptive equilibrium was

established. Initially, 0.025 g of the bV_2O_5 was added to a 50 mL solution of 95 mg/L MB and stirred in the dark for 3 h to ensure adsorptive equilibrium was reached. 3 mL aliquots were taken and filtered using a $0.45 \text{ }\mu\text{m}$ mixed cellulose-ester filter paper. The filtered aliquots were analyzed via UV–Vis spectroscopy to ensure that 20 mg/L MB indeed remained in solution. The solution was then transferred to a 50 mL reactor and irradiated using an artificial solar simulator at intensity of 700 W/m^2 for 1 h under continuous stirring, with 3 mL samples taken in a predetermined interval using a standard 10 mL syringe. The solar simulator was calibrated using a standard CMP6 Kipp & Zonen pyranometer with a spectral range of $285\text{--}2800 \text{ nm}$. The MB in collected samples was analyzed using liquid UV–Vis Spectroscopy (PerkinElmer Lambda 950 Spectrophotometer) at λ_{max} of 664 nm . Similar experiments were conducted using pristine $\alpha\text{-V}_2\text{O}_5$ (pV_2O_5) as the photocatalyst and a 20 mg/L MB was ensured at the start of the photodegradation test. The degradation percentage was calculated as:

$$\text{Degradation}(\%) = \frac{100 \cdot (C_0 - C_t)}{C_0} \quad (3)$$

where, C_0 is the initial MB concentration and C_t is the concentration of MB after time (t). From it, the degradation efficiency can be attained by simple subtraction from unity. We performed adsorption and photodegradation tests on neutral-charge quinoline yellow (QY) and anionic methyl orange (MO) for investigating the effect of charge of the dye.

3. Results and discussion

3.1. Adsorption of reduced 'black' V_2O_5 catalysts

Although no notable change to the morphology of the V_2O_5 material was observed upon reduction, the obtained pore volume (V_p) of bV_2O_5 ($0.0524 \text{ cm}^3/\text{g}$) was higher by 12% than that of pV_2O_5 ($0.0468 \text{ cm}^3/\text{g}$) and correspondingly the pore diameter (L) was higher by 30% as shown in Table 1. The equilibrium adsorption capacity (q_e) was calculated using the below equation:

$$q_e = \left(\frac{C_0 - C_e}{m} \right) \times V \quad (4)$$

where C_0 and C_e are the initial and equilibrium concentrations of MB (mg/L), respectively, m is the mass of adsorbent (g), and V was the volume of solution (L). The equilibrium concentration was measured after 3 h of dark adsorption conditions. The adsorption capacities (mg/g) of solids prepared herein were compared with other adsorbents reported in the literature and based on data shown in Table 1, the order of adsorption capacity of these solids increases in the order of: Activated Carbon (AC) > Graphene Oxide (GO) > Carbon Nanotubes (CNT) > bV_2O_5 > pV_2O_5 . Interestingly, the normalized adsorption of the aforementioned solids with respect to their surface areas show a completely different behavior (see Fig. 2) whereby the normalized adsorption capacities (mg/m^2) are in increasing order as follows: bV_2O_5 > pV_2O_5 > GO > CNT > AC. Coupling this finding with the neutral-pH Zeta Potentials (mV) noted in Table 1, we deduce that the induction of surface O_v in reduced bV_2O_5 results in a highly negative surface charge, which makes suitable for

Table 1

Physical properties of pristine and black V_2O_5 in comparison to AC, CNT, and GO: surface area (S_{BET}), total pore volume (V_p), average pore diameter (L), adsorption capacities (q_e), and neutral-pH Zeta Potential.

Sample	S_{BET} (m^2/g)	V_p (cm^3/g)	L (nm)	q_e (mg/g)	Neutral pH Zeta Potential (mV)	Reference
pV_2O_5	3.2	0.047	30.9	25.0	-20.8	This work
bV_2O_5	3.0	0.052	40.2	75.6	-61.2	This work
AC	1688	1.04	2.5	270.3	-32	[60]
CNT	177	0.54	12.1	188.7	-58	
GO	32	0.11	17.3	243.9	-54	

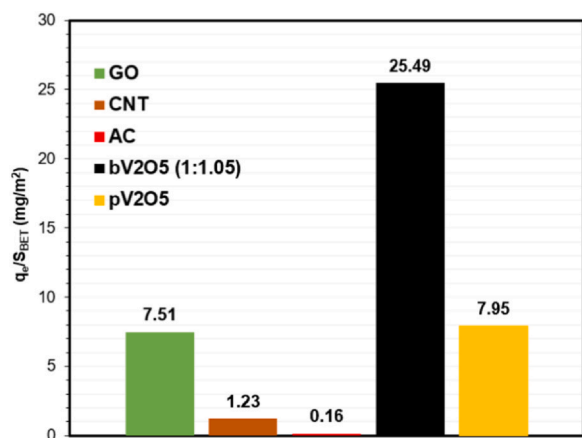


Fig. 2. Comparison of adsorption capacities of GO, CNT, AC, pV₂O₅, and bV₂O₅ normalized by BET surface area.

adsorbing positively charged cationic MB through very strong electrostatic forces of attraction. The high negative zeta potential in bV₂O₅ is generated through a larger density of surface OH⁻ binding from surrounding water. This could possibly be as a result of the high-density unoccupied d-orbitals transcended upon borohydride reduction of the metal oxide. It is the higher concentration of this negatively charged surface that facilitate the strong electrostatic interactions between the bV₂O₅ surface and cationic MB. It shall be noted that the vacant site, guided by V_o⁺ formation immediately after vacancy formation, is positively charged and in turn acts as an electron trap site – effectively allowing a net surface negative charge. This significant increase in the absolute Zeta Potential value of bV₂O₅ compared with pristine V₂O₅ is also indicative of a more homogeneously dispersed (low aggregation) bV₂O₅ in solution, which favors greater adsorption. This also supports the findings of an enhanced photoactivity of the bV₂O₅ compared to pV₂O₅ since MB adsorption is an elementary step of any photodegradation process.

3.2. Photocatalytic performance of reduced ‘black’ V₂O₅ catalysts

The photocatalytic degradation characteristics of different V₂O₅ samples were characterized by first allowing 3 h of dark adsorption conditions to level off at 20 mg/L of remaining MB in solution (after adsorption equilibrium is reached). Thereafter, the reactor was irradiated with 0.7 kW/m² of artificial visible light and sampled in 20-minute intervals. Both the effects of calcination environment and reduction ratio on the apparent photodegradation performance were investigated. First, the effect of initial calcination atmosphere was probed by calcinating the Vanadia precursor in Argon and in Vacuum. Vacuum calcination has reportedly been used to create intrinsic oxygen vacancies in other metal oxides [61]. bV₂O₅ (vacuum calcination) showed higher adsorption capacity compared to the sample calcinated in Argon. Interestingly, as shown in Fig. 3a, the photoactivity of the bV₂O₅ (Vacuum) sample showed initial sluggish kinetics, which could be attributed to the faster desorption kinetics upon irradiation due to heating effects. However, it shall be noted that an argon atmosphere was adopted during NaBH₄ reduction in order to present an inert atmosphere with no oxidizing agent; which would have otherwise lead to repopulation of newly formed O_v sites. Had the latter been undertaken, the catalyst performance in photodegradation would resemble that of pristine V₂O₅ which shows no O_v in its lattice. Second, the reduction ratio (V₂O₅: NaBH₄) was tuned to optimize the ratio of surface O_v – believed to enhance photoactivity. The concentration of surface O_v has been selectively increased using more hazardous reduction methods [62]. In this work, however, the concentration of surface to bulk O_v leading to the

highest photoactivity of V₂O₅ was found to be 1:1.05 under the physicochemical reduction scheme used. Correspondingly, the reduced sample with a higher NaBH₄ ratio (i.e. bV₂O₅ (1:1.25)) showed slower kinetics compared with bV₂O₅ (1:1.05) – indicative of a higher ratio of bulk to surface O_v in the bV₂O₅ (1:1.25) sample. It is worth noting that all 3 investigated bV₂O₅ samples reached the same removal percentage (C/C₀) of 93% after 60 min of visible light irradiation. The optimum bV₂O₅ (1:1.05) sample showing higher kinetics will hereby be referred to as bV₂O₅. One of the main areas that need further development in photocatalysis research is the standardization of reactors or testing setup. Thus, in an effort to justifiably compare the prepared bV₂O₅ materials with well-established photocatalysts (i.e., ZnO, TiO₂, black TiO₂), the same photodegradation performance testing was undertaken.

The degradation followed pseudo first-order reaction kinetic rates, as is depicted in Fig. 3b. The degradation rate constant was obtained from the slopes of curves in Fig. 3b, elucidated by using equation $-\ln(C/C_0) = kt$. The highest degradation rate was witnessed for the optimized bV₂O₅ sample ($k = 0.0408 \text{ min}^{-1}$) which is a 58-fold increase under visible light photodegradation rate compared with the pristine V₂O₅ sample. All bV₂O₅ samples achieved approximately 93% removal efficiency compared with 58.7%, 62.9%, and 81.3% for ZnO, P25 (TiO₂), and black TiO₂, respectively. Interestingly, the higher available surface oxygen density in V₂O₅ allows for the formation of more O_v per periodic cell compared to TiO₂. As will be elaborated on in later sections, the effective heterojunctioning between pristine and reduced V₂O₅ components in the final bV₂O₅ material employed allows for a clear enhancement in photoactivity. This effect is due to the reduced electron-hole recombination rate in the final bV₂O₅ material. It is worth noting that MB degradation was performed based on the prominent absorption peak of the monomer at 664 nm. However, oligomers of its dimmer and trimmer are difficult to break down due to stronger molar absorptivity from higher resonance which translates to higher chemical stability [63]. To this end, degradation intermediates of MB have been reported in several works which depict a multi-step degradation mechanism of the more complex initial MB molecule. Electrochemical impedance spectroscopy (EIS) in Fig. S10 showed that the impedance of bV₂O₅ is significantly reduced due to the increase of charge. The smaller the radius of the arc (charge transfer resistance – R_{CT}), the lower the ability to hinder transport of photogenerated carriers [64–66]. Charge inhibition properties attained from the Nyquist plot convey that photogenerated carriers could diffuse rapidly on the surface of bV₂O₅, in effect promoting reaction kinetics of the photogenerated carriers on the surface of the photocatalyst. Due to the Conduction Band Minimum (CBM) of bV₂O₅ being below that of the pristine counterpart, a photoexcited electron on a pV₂O₅ crystal that is heterojunctioned to a bV₂O₅ crystal will recombine at the CBM of bV₂O₅ – effectively acting as a trap state for photoexcited electrons of pV₂O₅ crystals.

The effect of the dye charge was examined using the optimum bV₂O₅ catalyst. Briefly, 3 h adsorption experiments were performed to ascertain the adsorption capacity of MB, QY, and MO atop bV₂O₅ such that dye concentration at the start of visible-light irradiation is maintained at a comparable 20 mg/L. Table S3 summarizes the respective adsorbed concentrations of charged and uncharged dyes atop bV₂O₅, whereby it is clear to realize that the anionic nature of bV₂O₅ allows for large concentrations of MB to be adsorbed. Contrarily, small amounts of QY and MO were adsorbed. At first glance, a larger amount of QY than MO is expected to be adsorbed due to its neutral charge compared to electrostatic repulsions from bV₂O₅-MO interactions. However, the large size of QY molecules may sterically hinder them from being adsorbed compared to smaller MO molecules. Nonetheless, the effect of charge on photodegradation is reflected in Fig. 3c, whereby degradation efficiency of QY in 1 h of visible light was approximately 82%, which is slightly lower than

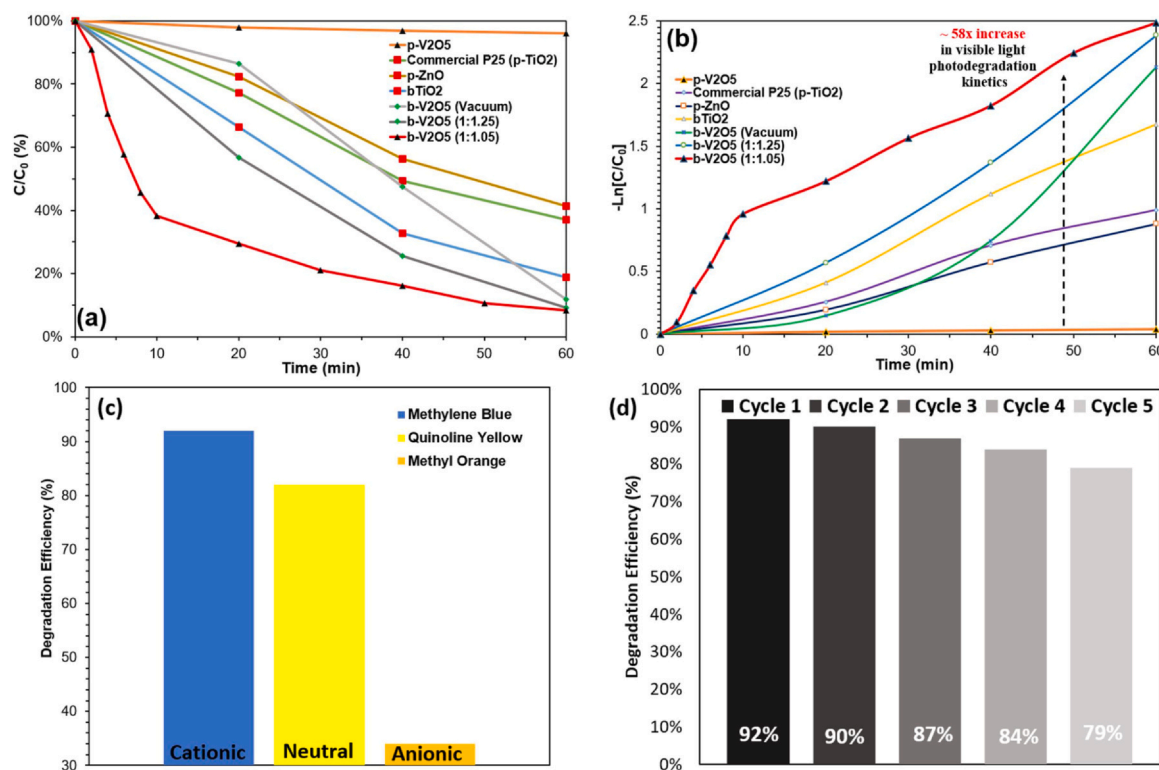
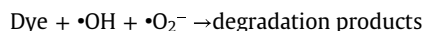
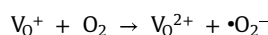
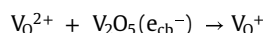
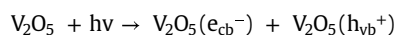


Fig. 3. (a) Visible light (0.7 kW/m^2) photodegradation of MB (20 mg/L), (b) pseudo first-order reaction kinetics of pV₂O₅, Commercial P25 (p-TiO₂), pZnO, bTiO₂, bV₂O₅ (Vacuum), bV₂O₅ (1:1.25), and bV₂O₅ (1:1.05), (c) degradation efficiency of bV₂O₅ (1:1.05) in 20 mg/L methylene blue (MB), quinoline yellow (QY), and methyl orange (MO), and (d) attained photodegradation efficiency over five cycling performance experiments (visible-light irradiation time is 60 min for each cycle, the amount of MB injected at each cycle increased MB concentration by $\sim 0.25 \text{ mM}$). Catalyst loading for all experiments was maintained at 0.5 g/L .

that of MB (92%) but much higher than that attained for MO (34%) – see Fig. S7. Also, MB degradation rate was approximately 1.4 times faster than QY and 4.7 times faster than MO using bV₂O₅ (Table S4). This could be because cationic dyes such as MB might have a stronger affinity for radicals formed under light irradiation, so that their photocatalytic degradation occurs at a higher rate compared to neutral charged QY. Further, several previous reports have conveyed the complex multi-step degradation mechanism of some of the discussed azo dyes such as MB and MO through TMO-based photodegradation [67,68]. This comes to show that a dedicated future study on the degradation mechanism of MB, MO, and QY using oxygen deficient TMO photocatalysts may be necessary to fine tune structural parameters which may enhance degradation of intermediates exhibiting higher stabilities against radical-induced degradation than the original molecule. This can be attained through employing gas chromatography mass spectrometers (GC-MS) for identifying the respective degradation intermediates, which may be different than those found from photodegradation through pristine TMO photocatalysts [69]. The photocatalyst stability towards photodegradation of MB has been examined by performing recyclability tests on bV₂O₅, as shown in Fig. 3d. The attained maintenance of performance has been ensured through which degradation efficiency drops by approximately 10% after 5 cycles. This partial drop in efficiency may partly be attributed to minor errors in the recyclability experiments which propagate towards catalyst loadings being smaller than the 0.5 g/L in the initial experiment.

The significant improvement in photoactivity of the bV₂O₅ sample compared to the pristine V₂O₅ can in part be attributed to induced oxygen vacancies and surface defects. The oxygen vacancies are formed when oxygen atoms are removed from the lattice structure during the reduction process with NaBH₄, initially leaving positively charged defects on the surface. The proposed mechanism for photocatalytic dye degradation using bV₂O₅ is similar to that

reported for its pristine counterpart [70]. V₀²⁺ represents the positively charged surface oxygen vacancies at the time of induction.



The oxygen vacancies on the surface act as trapping sites for the excited electrons, capturing the electrons and lowering electron – hole pair recombination. As a result, these surface oxygen vacancies result in the formation of an intermediate energy level between the conduction and valence energy bands, effectively narrowing the band gap and further enhancing photocatalytic properties in the visible light region [71]. A photodegradation schematic for the bV₂O₅ photocatalyst is conveyed in Fig. 4 highlighting the type-II heterojunction between pristine and reduced Vanadia surface. Further, it provides insight that the attained reduced V₂O₅ possesses a Z-scheme mechanism, whereby a photoexcited e^- from the VB of pV₂O₅ migrates to the CB on the same crystal, followed by transference to the VB of a coupled black V₂O₅ crystal acting as a trap state [72,73]. The same e^- can then be photoexcited with less energy, namely visible-light photons, towards the CB of the latter crystal to participate in formation of a superoxide radical.

Surface oxygen vacancy sites with trapped photoexcited electrons can act as active sites for the adsorption of an O₂ molecule from the catalyst environment. The trapped electron is transferred to the O₂ molecule, generating the superoxide radical anion ($\bullet\text{O}_2^-$), which is a strong oxidizing agent, and enhances the degradation of the organic dye [74]. This in effect increases the available

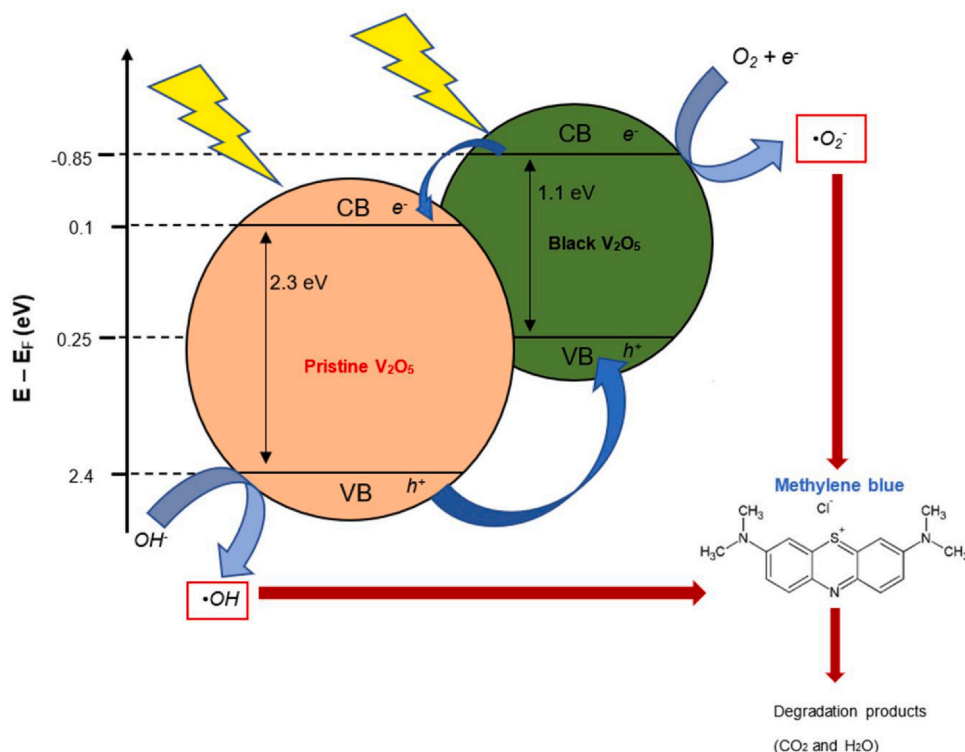


Fig. 4. Schematic for visible-light photodegradation of MB with bV_2O_5 composed of pristine and reduced surface heterojunction. Bandgap edges are based on DFT calculation results.

surface-sites for radical formation. The positively charged holes in the valence band react with the hydroxide (OH^-) ions in solution to form the hydroxide radicals ($\bullet\text{OH}$). The hydroxide radicals and the superoxide anion radicals then react with the organic dye to form the degradation products. The individual contributions of both oxidizing species, $\bullet\text{O}_2^-$ and $\bullet\text{OH}$ were evaluated via degradation experiments involving reactive oxidative species (ROS) scavengers, so as to determine the main ROS involved in the degradation mechanism, the results of which are discussed in the section to follow.

3.3. Textural and crystallinity properties of V_2O_5 photocatalysts

Scanning Electron Microscope (SEM) images pV_2O_5 and bV_2O_5 samples are shown in Fig. 5a, b. As is seen, the pristine sample (Figs. 5a, S1) consists of highly faceted microscale brick-shaped structures with varying sizes and relatively smooth surfaces. Similarly, the reduced black vanadium (V) oxide sample (Figs. 5b, S2) shows similar microscale brick shaped structures. Interestingly, however, it is noticeable that the surfaces of the 'microbricks' are not smooth and an apparent growth of oriented nanoscales is witnessed. With close inspection in Fig. 5b, it can be observed that the nanoscale particles have grown perpendicular to the surface. This is a quite enthralling morphological modulation upon reduction, since the displayed nanoscales were found to be the thermodynamically favored defect surface structure based on DFT calculations. Briefly, the results of DFT calculations indicated that the predominant (001) facet obtained from XRD results of the bV_2O_5 sample was found to have the highest degree of configurational change upon reduction. This is confirmed by both HRTEM images in Fig. 5c, d whereby a clear (001) growth facet is witnessed and indicated by lattice fringe spacing of 0.43 nm. Oxygen vacancy sites are highlighted in Fig. 5d atop the bV_2O_5 surface. Moreover, the distortion found at the bottom of the HRTEM image of bV_2O_5 represents a facet interface with (110) facets prevalent from XRD characterization in Fig. 5f. EDS analysis in Fig. 5e on the reduced sample reveals that Vanadium and Oxygen

predominantly constitute the surface, with a very small amount of Sodium (3 wt%) in bV_2O_5 – corresponding to the $\text{Na-V}_2\text{O}_5$ phase attained from reduction impurities. The presence of Sodium is a result of the physicochemical reduction procedure with the borohydride sodium salt. The reduced surface was found to be negatively charged upon reduction due to vacancy formations leading to high-density unoccupied d-orbitals, which lead to a larger density of surface OH^- binding from surrounding water. A degree of monovalent cationic sodium gets thermodynamically intercalated to the resultant surface and is believed to play a subtle, but important role. Previous reports on the effect of intercalated Na^+ in a photocatalyst's crystal lattice indicate the enabling of neighboring photogenerated electrons to transfer along the bridge-Na sites [75,76]. This phenomenon expedites adequate separation of photogenerated electron-hole pairs and increase lifetime of photogenerated carriers. Thus, it is our belief that upon borohydride reduction, the modest degree of $\text{Na-V}_2\text{O}_5$ phase in bV_2O_5 inhibits the electron-hole recombination rate, which aids in improving photodegradation efficiency.

Wide-angle XRD patterns of pV_2O_5 and bV_2O_5 provided in Fig. 5f show the characteristic orthorhombic Pmmn space group. Clearly, pV_2O_5 phases are established from the predominant polar (001) and nonpolar (110) facets at 20.31 and 26.15 2θ ($^\circ$), respectively. Peak positions are in seamless agreement with Powder Diffraction File (PDF) 04-007-0398 [77]. Specific surface energy results obtained by DFT calculations predicted an expected slightly lower energy for the (110) surface. However, upon reduction the oxygen vacant (O_v) polar surface seems to be more stable. Nevertheless, a clear diminishment in peak intensity is observed in the reduced bV_2O_5 sample. Interestingly, the bV_2O_5 sample shows the presence of two new phases – namely V_4O_9 [78] and $\text{Na-V}_2\text{O}_5$ [79]. The V_4O_9 phase corresponds to the creation of O_v atop the surface, and the $\text{Na-V}_2\text{O}_5$ is believed to be due to electrostatic attraction between Na^+ and the negatively charged oxygen vacant surface of bV_2O_5 . Although the V_2O_5 phase appears to have a similar degree of presence of both polar (001) and

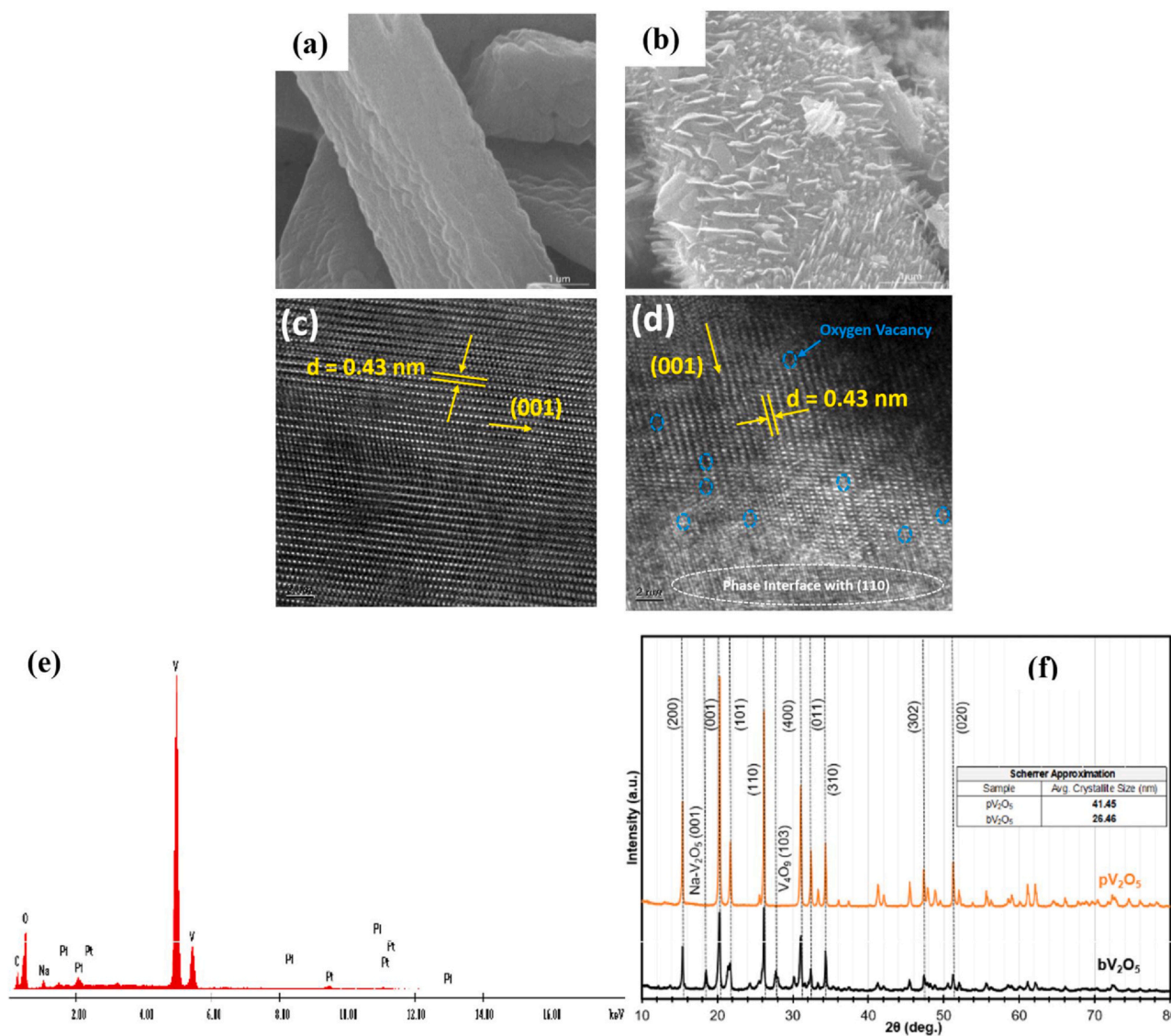


Fig. 5. SEM and HRTEM images of as-prepared (a, c) pV₂O₅ and (b, d) bV₂O₅ photocatalysts, (e) EDS spectra of bV₂O₅ (Pt peaks are due to Pt-coating of powder samples), and (f) wide-angle XRD patterns of pV₂O₅ and bV₂O₅ with average Crystallite Sizes (nm) for each.

nonpolar (110) facets, the intense peak at $18.45\ 2\theta$ ($^{\circ}$) corresponds to the polar (001) facet, thus resulting in a dominating polar surface for bV₂O₅. Furthermore, the Scherrer approximation was used to determine the average crystallite size (D) for both samples. The Scherrer constant was chosen to be 0.9 – for spherical crystallites – approximated from HRTEM images in Figs. S5 and S6. Expectedly from previous reduction work using the employed physicochemical reduction technique, a decrease in crystallite size is endured upon reduction – namely from 41.45 to 26.46 nm between pristine and bV₂O₅, respectively. This considerable decrease of approximately 41% in crystal sizes suggests a large volume fraction of V₂O₅ is transformed to another phase, which is not corroborated by XRD or Raman analyses. Thus, this notable decrease in crystallite sizes may be in part an artifact from XRD peak broadening due to increased strain distribution as a result of defect formation upon borohydride reduction. Since the reduced V₂O₅ material is strained, we appropriated the Williamson-Hall method to better approximate crystallite sizes since it factors for strain contributions. Briefly, crystallite size (d) can be obtained from the intercept of the resultant plot of $\beta\cos(\theta) = (0.9\ \lambda/d) + 2A\epsilon\sin(\theta)$, whereby λ is the CuK α radiation wavelength (1.5406 Å), β the peak width at the half maximum (in Rad), θ the Bragg angle, and ϵ and A are constants with accepted values of

unity [80]. Based on this, pV₂O₅ and bV₂O₅ yielded crystallite sizes of 43.2 and 35.3 nm, respectively, which suggests an 18% decrease in crystal size upon strain induction through O_v formation. Nonetheless, a crystallite size greater than 20 nm tends to be sufficient in suppressing electron-hole recombination through a large enough charge migration distance [81].

3.4. Surface microenvironment of V₂O₅ photocatalysts

Upon reduction of pristine Vanadia, a notable orange to black color change was observed. This can be attributed to the newly generated surface defects, oxygen vacancies, and lower order oxidation states of vanadium (i.e. V³⁺). To probe the changes in surface chemical states and electronic structures after reduction, XPS measurements were undertaken on both the pristine and bV₂O₅ samples for comparison. V 2p spectra analysis of both the pristine and reduced samples in Fig. 6a show notable difference upon deconvolution of the peaks. Initially, ground state V_{3/2}⁵⁺ and V_{1/2}⁵⁺ corresponding to 517.2 eV and 524.4 eV, respectively, are evidently the two manifesting peaks in the V 2p spectra. These values are in exceptional agreement with previously measured Vanadia oxidation states of V₂O₅ [82]. Interestingly, upon reduction, the prominent peak at

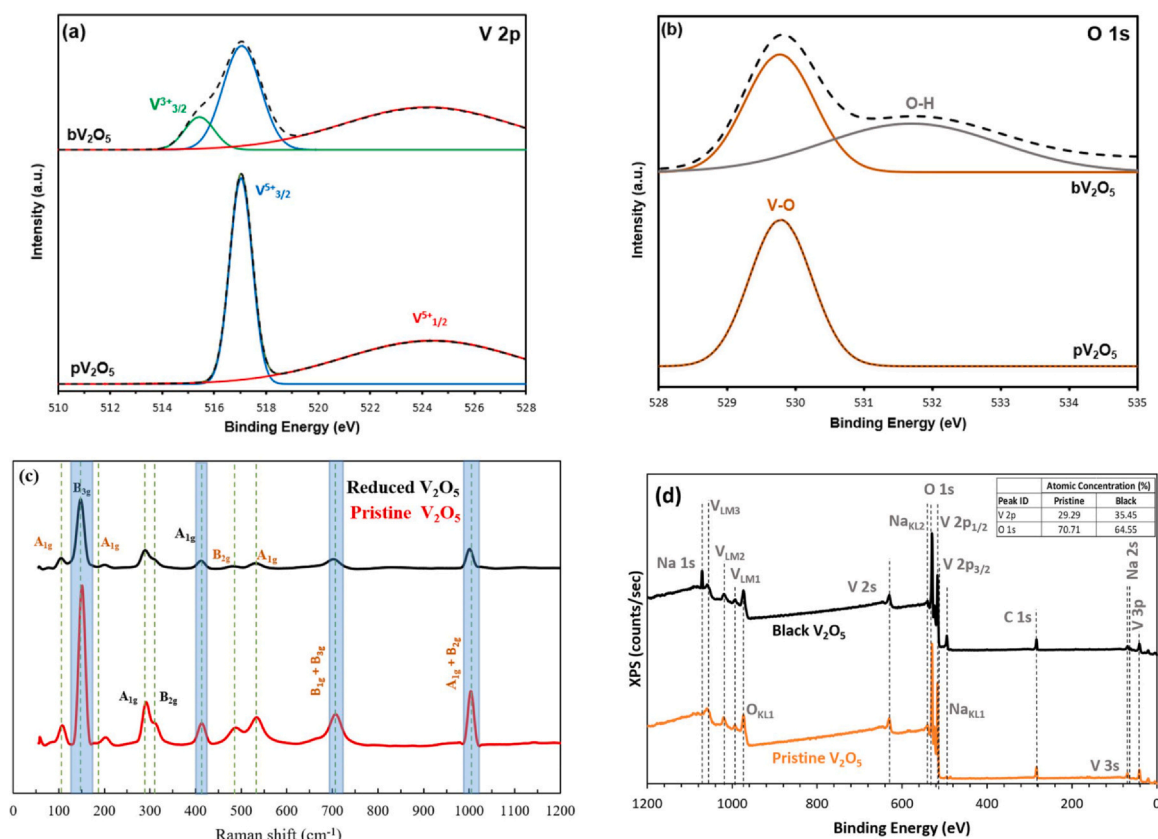


Fig. 6. XPS spectra of (a) V 2p and (b) O 1s of pristine V_2O_5 , and black (reduced) V_2O_5 , (c) Raman spectra of pristine and reduced V_2O_5 , and (d) full survey XPS scan of as prepared both pristine and black V_2O_5 .

517 eV shows a lower intensity for bV_2O_5 than that for pV_2O_5 due to the formation of a high degree of the lower oxidation state vanadium, V^{3+} , corresponding to a binding energy of 515.4 eV. It is hypothesized that active hydrogen generated from borohydride thermal decomposition during reduction reacts with lattice oxygens, forming oxygen vacancies. The formation of lower oxidation states of Vanadium such as V^{3+} results from excess electrons available to reduce the highly oxidized V^{5+} [83]. V_4O_9 phase confirmed earlier through XRD analysis of the bV_2O_5 catalyst, is not evident from an oxidation state standpoint in the XPS analysis through V^{4+} or V^{2+} states. A possible explanation for this relates to vacant oxygen sites having an oxidation state of O^{2-} at the time of vacancy introduction. To allow for charge neutrality, V^{3+} states form instead of V^{4+} or V^{2+} . $Na-V_2O_5$ phase is in good agreement with the V^{5+} states still present in the reduced V_2O_5 spectra. Although the presence of surface V^{3+} upon reduction is indicative of O_v formation, deconvolution of the O 1s spectra in Fig. 6b overtly clarifies the presence of hydroxide surface groups, typically associated with surface defects and oxygen vacancies [84].

To further confirm the presence of oxygen vacancies in the reduced V_2O_5 sample and investigate the crystal structure and surface defects, Raman spectroscopy under excitation wavelength of 532 nm was undertaken and the spectra are presented in Fig. 6c. In the reported range of 40–1200 cm^{-1} , several representative V_2O_5 peaks are evident; namely at 106 cm^{-1} , 149 cm^{-1} , 202 cm^{-1} , 290 cm^{-1} , 310 cm^{-1} , 415 cm^{-1} , 706 cm^{-1} , and 1003 cm^{-1} , which is in agreement with data reported in the literature [85]. The reduced sample shows a slight shoulder peak at 407 cm^{-1} corresponding to the minute surface presence of V_4O_9 phase that was confirmed from XRD. The highlighted peaks in Fig. 6c convey a Lorentzian fit showing an apparent peak broadening and negative shifting in the B_{3g} mode of in-phase oscillation of vanadium, $O_{(2)}$, and $O_{(3)}$ atoms along the

b-axis for the reduced V_2O_5 sample. A similar phenomenon is witnessed for the A_{1g} mode at 415 cm^{-1} , ($B_{1g} + B_{3g}$) mode at 706 cm^{-1} , and ($A_{1g} + B_{2g}$) mode at 1003 cm^{-1} , corresponding to $V-O_{(3)}-V$ angle-bending, asymmetric stretching of $V-O_{(2)}-V$, and stretching vibrations of the vanadyl bonds, respectively. This is indicative of the creation of lattice distortions because of oxygen vacancy formation. Furthermore, the full-width half maximum (FWHM) of the main Raman peak at the B_{3g} mode shows an increase from the pristine to the reduced sample, is another indication of a high presence of surface oxygen vacancies [86–88]. The comparison of Raman spectra between the pristine and reduced V_2O_5 samples shows no new presence of Raman peaks corresponding to other prominent phases of vanadium oxides, which in turn supports the postulation that the $\alpha-V_2O_5$ phase is maintained upon reduction. This finding corroborates the black coloring of bV_2O_5 to induced surface defects and oxygen vacancies, and not the formation of dark-green colored phases such as V_3O_7 and V_2O_3 . Furthermore, phase transformation of V_3O_7 to V_2O_5 has been previously reported in literature under Raman analyses when using laser settings of 300 W/ cm^2 and incident power of 20–30 mW. In this case, we have utilized a laser power of 5 mW using the DXR Raman Microscope employed in analysis, which is well below the limit found to cause such phase transformations between vanadium oxides. Confirmation of the sample purity and maintenance in identity was further ensured through performing full XPS surveys of both pristine and reduced counterparts of the as prepared V_2O_5 photocatalysts, as seen in Fig. 6d. Further, the inset confirms that the concentration of oxygen within the reduced metal oxide has been reduced due to formation of oxygen vacancies upon the physicochemical reduction.

DRS was employed on both pristine and black V_2O_5 as shown in Fig. S8a to evaluate the behavior of bV_2O_5 and pV_2O_5 under visible light and it shows the clear enhancement of visible-light absorption

by the reduced sample. Lack of d–d orbital transitions in the 600–800 nm region is indicative of a high oxidation state of vanadium, V^{5+} , because the d–d transitions predominantly depend on the presence of V^{4+} states. Furthermore, the pristine V_2O_5 presented in Fig. S8a clearly depicts the anticipated two intense absorption shoulder peaks at 344 and 452 nm, corresponding to charge transfer bands whereby transitions $a_2(p) - b_2(xy)$ and $b_1(p) - b_2(xy)$ comprising a V^{5+} and four equatorial oxygen atoms [89]. Interestingly, a clear peak reduction in the representative V^{5+} shoulder peaks at 344 and 453 nm in the bV_2O_5 absorption spectrum indicates the presence of lower oxidation states of vanadium. This can be attributed to excess electrons available to reduce surface V^{5+} . Nevertheless, bV_2O_5 shows a lucid absorption of UV, visible and near-IR wavelengths, which is highly desired for photocatalytic utilization of visible and IR range photons which are much more abundant in the solar spectrum than the high energy UV photons.

The bandgap (E_g) of the materials was systematically calculated under the governing Tauc's relationship [90]: $\alpha h\nu = A(h\nu - E_g)^n$ whereby α is the absorption coefficient, A is a constant, h is Planck's constant, ν is the photon frequency, and n equals 3/2 for materials with direct forbidden bandgaps – confirmed later for V_2O_5 by DFT. Fig. S8b shows extrapolated values of 2.35 and 1.35 eV for pristine and bV_2O_5 , respectively. Other methods such as Kubelka-Munk can also be appropriated for approximating the experimental bandgap of the semiconductor [91]. A conundrum posing itself then becomes, what is the origin of the bandgap reduction in bV_2O_5 . Raman analysis in Fig. 6c indicated a lack of other vanadium oxide phases with lower bandgaps (i.e. V_2O_3 , VO_2 , etc.), which can contribute to an apparent bandgap reduction if present in bV_2O_5 . We propose undertaking a future study aiming at identifying the presence of Urbach energy (E_u) and weak absorption band-tails (E_t) formed due to defect propagation (i.e. sub-surface vacancies) in the reduced oxide's bulk. As will be shown from DFT calculations, the formation energy of sub-surface vacancies is too demanding to be spontaneous, and as

such we deem the formation of band-tails causing bandgap reduction unlikely. Furthermore, DFT analysis will show that favorable formation enthalpies of some surface oxygen vacancies do result in a bandgap reduction. Thus, we postulate that the reduction in bandgap and consequential enhancement in visible light utilization is a result of oxygen vacancies present in the bV_2O_5 samples.

3.5. DFT calculations

Fig. 7a shows the optimized structure of pristine V_2O_5 for both (110) and (001) exposed facets. Band edges of all investigated systems including, but not limited to, pV_2O_5 (110) and (001) as well as their reduced counterparts. Eigenvalue bandgaps, which are essentially the difference in KS eigenvalues between lowest and highest occupied states, have been used in Fig. 7b to determine the theoretical bandgap edge for both the pristine and (001) bV_2O_5 systems. We recognize that some limitations (i.e. lack of derivative discontinuity in the XC functional [92]) arise from using KS eigenvalues to theoretically calculate the bandgap, and probably other more accurate “beyond DFT” methods may be needed. However, this method indicates the emergence of an interesting heterostructure which can be categorized as a staggered (type-II) heterojunction bandgap. Heterostructures with type-II band alignment were sought after in photocatalysis since the energy gradient at the heterostructure's interface could aid in electron-hole separation and localize electrons and holes on different sides of the pV_2O_5/bV_2O_5 heterostructure [93]. This in turn can shed more light on the substantial apparent improvement in photoactivity of the bV_2O_5 samples compared to their pristine counterpart.

Fig. 7b depicts the aforementioned staggered (type-II) heterostructure whereby energy levels of the Valence Band Maximum (VMB) and Conduction Band Minimum (CMB) are located at -6.8947 eV and -4.6017 eV, respectively for pV_2O_5 , and -4.7329 eV and -3.6487 eV, respectively for bV_2O_5 versus vacuum. This corresponds to theoretical

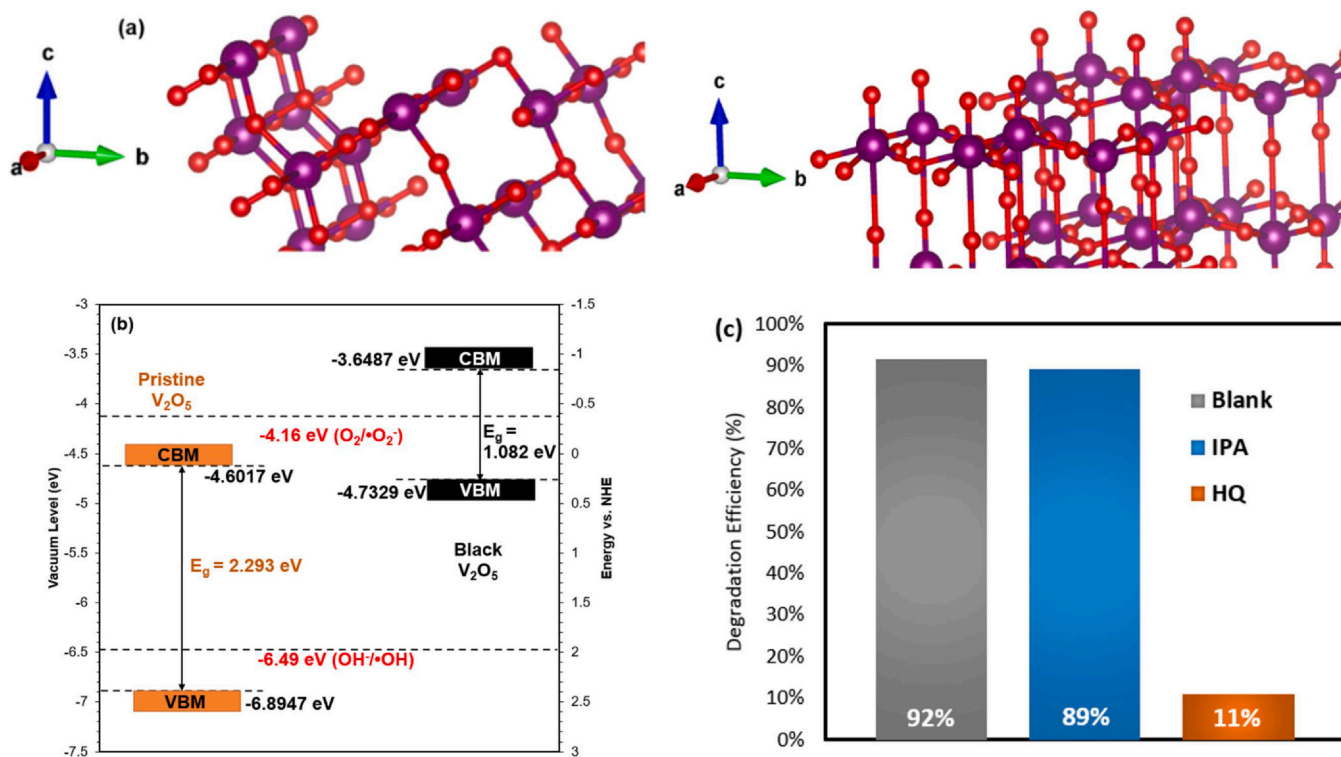


Fig. 7. (a) Fully relaxed structure of the nonpolar (110) (right) and (001) (left) pristine V_2O_5 , (b) calculated band edge positions of pristine and black V_2O_5 with respect to Vacuum Level and with respect to NHE; numerical values in (b) are with respect to Vacuum Level, and (c) the effects of a series of scavengers on the degradation efficiency of MB (IPA – isopropyl alcohol, HQ – hydroquinone, dosage of scavengers = 0.1 mmol/L, visible-light irradiation time is 60 min for each experiment).

bandgaps of 2.293 eV and 1.082 eV for pristine and bV₂O₅, respectively. Since the GGA method used here is known to slightly underestimate bandgap positions, the enhanced photoactivity of the reduced bV₂O₅ sample (containing both surface pristine and black V₂O₅ crystallites) may also be attributed to the facile thermodynamics of superoxide radicals ($\bullet\text{O}_2^-$) being the ROS generated for photocatalytic contaminant degradation. Although the hydroxy radical ($\bullet\text{OH}$) energy is present within the bandgap of pV₂O₅, it does not contribute to the observed photodegradation because of the innate poor photoactivity of pristine α -V₂O₅. Fig. 7c depicts the photodegradation efficiency of bV₂O₅ under IPA and hydroquinone scavengers for sequestering hydroxyl and superoxide radicals, respectively. The results confirm that under sequestering or scavenging superoxide radicals during photocatalysis of bV₂O₅, the photodegradation efficiency nearly ceases completely.

The effective Hubbard ($U_{\text{eff}} = U - J$) correction term which integrates intra-atomic Coulombic (U) and exchange (J) terms in the one-parameter U_{eff} term was determined to be 3 eV for both the vanadium 3d orbital and the oxygen 2p orbital (i.e. $U_{\text{eff-d}} = U_{\text{eff-p}} = 3$ eV). Optimization results that yielded the utilization of the aforementioned U value are provided in Table S2. The utilization of this GGA+ U approach results in a calculated bandgap value of 2.293 eV, which is a minute 2.5% underestimation of the experimentally determined value of 2.35 eV. Experimentally determined lattice parameters obtained through high refinement of XRD phases for both pristine and black V₂O₅ resulted in the same cell parameter values for both samples, namely $a = 11.516$ Å, $b = 3.565$ Å, and $c = 4.373$ Å. This compares very well with the theoretically obtained parameters for pristine and black V₂O₅ systems, which are $a = 11.527$ Å, $b = 3.614$ Å, and $c = 4.614$ and $a = 11.519$ Å, $b = 3.592$ Å, and $c = 4.582$ Å, respectively. Thus, the theoretical predictions of the structure are consistent with the experimental findings of the synthesized materials. Furthermore, given the high surface density of available oxygen sites in pV₂O₅ for reduction (1, 2, and 3 coordinated oxygen types), specific formation energies for each available oxygen type was calculated. The results in Fig. 8a show that all occurrences for oxygen vacancy formation are endothermic – requires energy input and is not spontaneous. Further, we find that the 2-Coordinated (2-C) and 1-Coordinated (1-C) oxygens are more thermodynamically favored in (110) and (001) facets, with formation energies of 0.70 and 0.74 eV per vacancy, respectively.

Charge density calculations in Fig. 8b and c were undertaken the top parallel plane to the surface where vacancies were introduced in (110) and (001) bV₂O₅, respectively. Interestingly, the introduction of a 2-C O_v in the nonpolar (110) facet of V₂O₅ does not impose a substantial surface rearrangement. Fig. 8b shows charge density grouping between pristine and black (110) V₂O₅ to be similar, with the main aberration occurring at the local coordination of atoms around the 2-C O_v. On the contrary, however, as can be seen in Fig. 8c, the relaxation of a polar (001) V₂O₅ surface with a 1-C O_v initial configuration results in the other 1-C oxygen on the neighboring surface vanadium to transition into a bridging (2-C) oxygen between the two vanadium atoms. Moreover, this stable rearrangement allows for a nudging of the surface layer approximately 1.25 Å above the initial pristine V₂O₅ surface plane pertaining to the local region around the 1-C O_v site. Neighboring grouping in (001) surface subdues by a similar distance below the initial surface plane. Thus, it can be surmised that the introduction of oxygen vacancies in the stable polar Vanadia facet results in a higher degree of surface defects compared to the nonpolar (110) facet. Expectedly, the specific surface energy of the (110) facet was approximately 22% lower than that of the polar (001) facet. However, upon reduction a lower specific surface energy of the (001) facet with the 1-C O_v – namely $3.05 \text{ eV } \text{\AA}^{-2}$ – is obtained. The aforementioned value is 6% lower than that of the 2-C O_v (110) system, having a specific surface energy of $3.23 \text{ eV } \text{\AA}^{-2}$. On average, the specific surface energies of reduced (110) and (001) bV₂O₅ are 3-fold higher than that of their pristine counterparts. This aids in the interpretation of the substantial performance enhancement in photoactivity of the reduced samples.

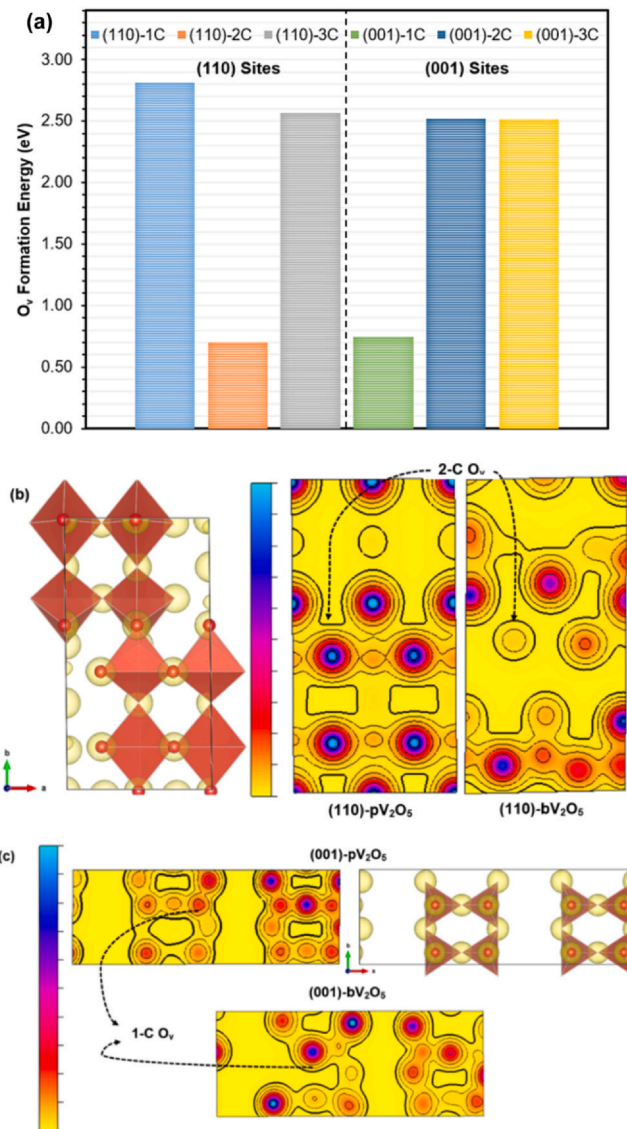


Fig. 8. (a) Oxygen vacancy formation energy (eV) per site on (110) and (001) bV₂O₅, and charge density representation of (b) (110) systems, and (c) (001) systems; color bar scale from -2.558×10^{-2} (yellow) to 1.202 (cyan) e/Å³.

The electron band structure for all systems investigated – both pristine and reduced – conclusively confirm an indirect bandgap which is intrinsic to V₂O₅. Total and Projected Density of State (T/PDOS) calculations were performed with a refined mesh. It shall be noted that the y-axis range in Fig. S9a and S9c is ± 50 (eV), and that in Fig. S9b and S9d is in the range of ± 6 (eV). This is expected, due to the larger contribution to TDOS in the ground state from higher populated orbitals of vanadium (d-orbitals) and oxygen (p-orbitals). Fig. S9a and S9b show the T/PDOS for pristine V₂O₅. The difference between VBM and CBM here gave very good agreement with the experimentally determined bandgap, which was 2.35 eV. The hybridization between the 2p and 3d orbitals of oxygen and vanadium, respectively, in the VB region confirms the strong covalent character in V–O bonds. The VBM in pV₂O₅ mainly originates from the O p states, and the contribution of the V d states is more notable farther away from the Fermi level.

Contrarily, the CBM is contrived predominantly from the donation of V d states. Fig. S9c and S9d, belonging to the (001) bV₂O₅ with a 1-C O_v has a remarkable similarity to all other systems investigated with oxygen vacancies, both for polar (001) and nonpolar (110) facets. Fig. S9c shows a very high occupation of V d states at the

VBM of bV_2O_5 , which are hybridized with O 2p orbitals, indicative of a well-maintained covalent bonding and stability of the reduced Vanadia material. Moreover, the introduction of newly formed electronic states near the Fermi level are rather interesting. This results in reducing the bandgap for the bV_2O_5 systems. It shall be noted that the obtained averaged bandgaps for the six different systems are in good agreement with the experimentally determined bandgap for bV_2O_5 of 1.35 eV. The higher occupation of transition states near the Fermi level allows for CBM to be more energetically available for photochemical reactions, compared with the pristine counterpart.

4. Conclusion

In this work, successful rational design and fabrication of a novel 'black' V_2O_5 (i.e., bV_2O_5) material that is photoactive under visible light was achieved via the utilization of an environmentally benign physiochemical technique on pristine V_2O_5 . Surface defects and oxygen vacancies in bV_2O_5 led to lowering the apparent experimental bandgap from 2.35 to 1.35 eV. Nyquist plots attained from EIS prove that the reduced sample, namely bV_2O_5 , exhibits charge transfer resistances much lower than its pristine counterpart. The heterojunction between surface pV_2O_5 and bV_2O_5 crystals on the same homogeneously dispersed microstructure allows for the creation of effective trap states. The modest degree of intercalated Na^+ in bV_2O_5 - introduced through $NaBH_4$ reduction - is believed to facilitate neighboring photogenerated electrons to transfer along the bridge-Na sites. Both these aid in inhibiting the electron-hole recombination rate, which enhances visible light photodegradation kinetics. The optimized bV_2O_5 photocatalyst was confirmed to actively achieve 92% MB photodegradation in 1 h under 0.7 kW/m^2 visible-light intensity, after reaching adsorption equilibrium (capacity = 75 mg/L MB) without light illumination. High adsorption capacities for cationic dyes, such as MB, coupled with rapid photodegradation kinetics promotes the developed bV_2O_5 photocatalyst towards further testing in applications involving photocatalytic water remediation, and as a dopant for other applications such as water splitting. Experimentally confirmed scavenging tests revealed that it is superoxide radicals which contribute to the attained photoactivity of the reduced sample.

A DFT+U approach was utilized to probe stability and redistribution of charge density upon reduction. It was found that the introduction of oxygen vacancies atop the polar (001) facet is highly stable and thermodynamically favorable compared to the nonpolar facets. A staggered (type-II) heterostructure between pristine and reduced V_2O_5 was observed from band edge positions, offering enhanced charge separation. Formation of new electronic states near the Fermi level upon reduction was confirmed by the comparison of PDOS plots of pristine and black Vanadia. The rational approach undertaken in this work to develop and investigate the novel black Vanadia is intended to lay the foundation for similar approaches on a myriad of other metal oxides. It is our belief that an immense potential for further material development can be achieved through surface engineering of promising materials for application in different fields.

Associated content

SEM and HRTEM imaging, neutral-pH Zeta Potentials, XRD-attained lattice parameters of pristine and black V_2O_5 , O 1s and V 2p deconvoluted spectra of pV_2O_5 prepared under vacuum calcination, schematic representations of (110) and (001) pristine V_2O_5 slabs, DFT-attained bandgaps, lattice parameters, VBM and CBM under PBE approach and PBE+U approach with different U parameters, EIS Nyquist plots, liquid UV-Vis spectroscopy on photodegradation of MB, QY and MO dyes, adsorption capacities, photodegradation

percentages, and photodegradation kinetics of MB, QY, and MO, DRS and $(ah\nu)^{3/2}$ vs E_g (eV) plots of prepared catalysts, Total and Projected Density of States (T/PDOS) plots of pV_2O_5 and (001)-black V_2O_5 , and thorough material synthesis section on all prepared samples discussed.

CRediT authorship contribution statement

Ahmed Badreldin: Methodology, Conceptualization, Software, Data curation, Investigation, Visualization, Validation, Writing - original draft. **Muhammad Danyal Imam:** Formal analysis, Investigation, Validation, Writing. **Yiming Wubulikasimu:** Data curation, Writing. **Khaled Elsaid:** Data curation. **Aya E. Abusrafa:** Visualization. **Perla B. Balbuena:** Supervision, Conceptualization, Software, Writing - review & editing. **Ahmed Abdel-Wahab:** Conceptualization, Supervision, Project administration, Resources, Funding acquisition, Writing - review & editing.

Declaration of Competing Interest

The authors declare that they have no known competing financial interests or personal relationships that could have appeared to influence the work reported in this paper.

Acknowledgment

This study was made possible by a grant from the Qatar National Research Fund under its National Priorities Research Program award number NPRP12S-0131-190024 and Texas A&M University at Qatar's RRSg program. The paper's contents are solely the responsibility of the authors and do not necessarily represent the official views of the Qatar National Research Fund. Supercomputer resources from the Texas A&M University High Performance Computer Center at College Station, Texas, are gratefully acknowledged. Open access funding provided by the Qatar National Library.

Appendix A. Supporting information

Supplementary data associated with this article can be found in the online version at doi:10.1016/j.jallcom.2021.159615.

References

- [1] S. Fukuda, K. Noda, T. Oki, How global targets on drinking water were developed and achieved, *Nat. Sustain.* 2 (2019) 429–434.
- [2] T. Tamiji, A. Nezamzadeh-Ejehieh, A comprehensive study on the kinetic aspects and experimental design for the voltammetric response of a Sn (IV)-clin-optilolite carbon paste electrode towards Hg (II), *J. Electroanal. Chem.* 829 (2018) 95–105.
- [3] H. Derikvandi, A. Nezamzadeh-Ejehieh, Increased photocatalytic activity of NiO and ZnO in photodegradation of a model drug aqueous solution: effect of coupling, supporting, particles size and calcination temperature, *J. Hazard. Mater.* 321 (2017) 629–638.
- [4] N. Pourshirband, A. Nezamzadeh-Ejehieh, S.N. Mirsattari, The coupled AgI/BiOI catalyst: synthesis, brief characterization, and study of the kinetic of the EBT photodegradation, *Chem. Phys. Lett.* 761 (2020) 138090.
- [5] A. Fujishima, K. Honda, Electrochemical photolysis of water at a semiconductor electrode, *Nature* 238 (1972) 37–38.
- [6] Y. Badr, M. Mahmoud, Photocatalytic degradation of methyl orange by gold silver nano-core/silica nano-shell, *J. Phys. Chem. Solids* 68 (2007) 413–419.
- [7] K. Hossain, N. Ismail, Bioremediation and detoxification of pulp and paper mill effluent: a review, *Res. J. Environ. Toxicol.* 9 (2015) 113–134.
- [8] J. Nawrocki, Catalytic ozonation in water: controversies and questions. Discussion paper, *Appl. Catal. B Environ.* 142 (2013) 465–471.
- [9] M. Rafatullah, O. Sulaiman, R. Hashim, A. Ahmad, Adsorption of methylene blue on low-cost adsorbents: a review, *J. Hazard. Mater.* 177 (2010) 70–80.
- [10] S.-T. Liu, J. Huang, Y. Ye, A.-B. Zhang, L. Pan, X.-G. Chen, Microwave enhanced Fenton process for the removal of methylene blue from aqueous solution, *Chem. Eng. J.* 215 (2013) 586–590.
- [11] M. Shanmugam, A. Alsalmeh, A. Alghamdi, R. Jayavel, Enhanced photocatalytic performance of the graphene- V_2O_5 nanocomposite in the degradation of methylene blue dye under direct sunlight, *ACS Appl. Mater. Interfaces* 7 (2015) 14905–14911.

- [12] J.S. Kim, E. Kuk, K.N. Yu, J.-H. Kim, S.J. Park, H.J. Lee, S.H. Kim, Y.K. Park, Y.H. Park, C.-Y. Hwang, Corrigendum to "Antimicrobial effects of silver nanoparticles" [Nanomed. Nanotechnol. Biol. Med. 2007; 1: 95–101], Nanomed. Nanotechnol. Biol. Med. 10 (2014) e1119.
- [13] V. Kumaravel, M.D. Imam, A. Badreldin, R.K. Chava, J.Y. Do, M. Kang, A. Abdel-Wahab, Photocatalytic hydrogen production: role of sacrificial reagents on the evolution of oxide, carbon, and sulfide catalysts, Catalysts 9 (2019) 276.
- [14] H. Derikvand, A. Nezamzadeh-Ejehie, Synergistic effect of pn heterojunction, supporting and zeolite nanoparticles in enhanced photocatalytic activity of NiO and SnO₂, J. Colloid Interface Sci. 490 (2017) 314–327.
- [15] A. Badreldin, Y. Zakaria, S. Mansour, A. Abdel-Wahab, Surface treatment-controlled solvothermal synthesis of highly active reduced 1D titania with heterojunctioned carbon allotrope, Emerg. Mater. (2021) 1–14.
- [16] R. Atchudan, T.N.J.I. Edison, S. Perumal, D. Karthikeyan, Y.R. Lee, Facile synthesis of zinc oxide nanoparticles decorated graphene oxide composite via simple solvothermal route and their photocatalytic activity on methylene blue degradation, J. Photochem. Photobiol. B Biol. 162 (2016) 500–510.
- [17] N. Arabpour, A. Nezamzadeh-Ejehie, Modification of clinoptilolite nano-particles with iron oxide: increased composite catalytic activity for photodegradation of cotrimazole in aqueous suspension, Mater. Sci. Semicond. Process. 31 (2015) 684–692.
- [18] A. Peter, A. Mihaly-Cozmata, C. Nicula, L. Mihaly-Cozmata, A. Jastrzebska, A. Olszyna, L. Baia, UV light-assisted degradation of methyl orange, methylene blue, phenol, salicylic acid, and rhodamine B: photolysis versus photocatalysis, Water Air Soil Pollut. 228 (2017) 41.
- [19] X. Chen, L. Liu, Y.Y. Peter, S.S. Mao, Increasing solar absorption for photocatalysis with black hydrogenated titanium dioxide nanocrystals, Science 331 (2011) 746–750.
- [20] Z. Dohlević-Mitrović, S. Stojadinović, L. Luzzi, S. Aškrić, M. Rosić, N. Tomić, N. Paunović, S. Lazović, M.G. Nikolić, S. Santucci, WO₃/TiO₂ composite coatings: structural, optical and photocatalytic properties, Mater. Res. Bull. 83 (2016) 217–224.
- [21] H. Zhou, X. Sheng, J. Xiao, Z. Ding, D. Wang, X. Zhang, J. Liu, R. Wu, X. Feng, L. Jiang, Increasing the efficiency of photocatalytic reactions via surface micro-environment engineering, J. Am. Chem. Soc. 142 (2020) 2738–2743.
- [22] R. Atchudan, T.N.J.I. Edison, S. Perumal, R. Vinodh, Y.R. Lee, In-situ green synthesis of nitrogen-doped carbon dots for bioimaging and TiO₂ nanoparticles@ nitrogen-doped carbon composite for photocatalytic degradation of organic pollutants, J. Alloy. Compd. 766 (2018) 12–24.
- [23] I.N. Reddy, C.V. Reddy, J. Shim, B. Akkinapally, M. Cho, K. Yoo, D. Kim, Excellent visible-light driven photocatalyst of (Al, Ni) co-doped ZnO structures for organic dye degradation, Catal. Today 340 (2020) 277–285.
- [24] P. Thirukumar, R. Atchudan, A.S. Parveen, K. Kalaiarasan, Y.R. Lee, S.C. Kim, Fabrication of ZnO nanoparticles adorned nitrogen-doped carbon balls and their application in photodegradation of organic dyes, Sci. Rep. 9 (2019) 1–13.
- [25] R. Atchudan, T.N.J.I. Edison, S. Perumal, N. Karthik, D. Karthikeyan, M. Shanmugam, Y.R. Lee, Concurrent synthesis of nitrogen-doped carbon dots for cell imaging and ZnO@ nitrogen-doped carbon sheets for photocatalytic degradation of methylene blue, J. Photochem. Photobiol. A Chem. 350 (2018) 75–85.
- [26] V. Cristino, G. Longobucco, N. Marchetti, C. Caramori, C.A. Bignozzi, A. Martucci, A. Molinari, R. Boaretto, C. Stevanin, R. Argazzi, Photoelectrochemical degradation of pharmaceuticals at p25 modified WO₃ interfaces, Catal. Today 340 (2020) 302–310.
- [27] Y. Liu, W. Guo, H. Guo, X. Ren, Q. Xu, Cu (II)-doped V₂O₅ mediated persulfate activation for heterogeneous catalytic degradation of benzotriazole in aqueous solution, Sep. Purif. Technol. 230 (2020) 115848.
- [28] H. Abdullah, M.M.R. Khan, H.R. Ong, Z. Yaakob, Modified TiO₂ photocatalyst for CO₂ photocatalytic reduction: an overview, J. CO₂ Util. 22 (2017) 15–32.
- [29] C.B. Ong, L.Y. Ng, A.W. Mohammad, A review of ZnO nanoparticles as solar photocatalysts: synthesis, mechanisms and applications, Renew. Sustain. Energy Rev. 81 (2018) 536–551.
- [30] R. Saravanan, V. Gupta, E. Mosquera, F. Gracia, Preparation and characterization of V₂O₅/ZnO nanocomposite system for photocatalytic application, J. Mol. Liq. 198 (2014) 409–412.
- [31] A. Fujii, Z. Meng, C. Yogi, T. Hashishin, T. Sanada, K. Kojima, Preparation of Pt-loaded WO₃ with different types of morphology and photocatalytic degradation of methylene blue, Surf. Coat. Technol. 271 (2015) 251–258.
- [32] S.C. Pillai, P. Periyat, R. George, D.E. McCormack, M.K. Seery, H. Hayden, J. Colreavy, D. Corr, S.J. Hinder, Synthesis of high-temperature stable anatase TiO₂ photocatalyst, J. Phys. Chem. C 111 (2007) 1605–1611.
- [33] S.A. Ansari, M.M. Khan, M.O. Ansari, M.H. Cho, Nitrogen-doped titanium dioxide (N-doped TiO₂) for visible light photocatalysis, New J. Chem. 40 (2016) 3000–3009.
- [34] P. Periyat, K. Baiju, P. Mukundan, P.K. Pillai, K. Warriar, Aqueous colloidal sol-gel route to synthesize nanosized ceria-doped titania having high surface area and increased anatase phase stability, J. Sol Gel Sci. Technol. 43 (2007) 299–304.
- [35] G. Li, L. Chen, N.M. Dimitrijević, K.A. Gray, Visible light photocatalytic properties of anion-doped TiO₂ materials prepared from a molecular titanium precursor, Chem. Phys. Lett. 451 (2008) 75–79.
- [36] A. Badreldin, A.E. Abusrafa, A. Abdel-Wahab, Oxygen deficient cobalt-based oxides for electrocatalytic water splitting, ChemSusChem 14 (2021) 10–32.
- [37] K. Chi, X. Tian, Q. Wang, Z. Zhang, X. Zhang, Y. Zhang, F. Jing, Q. Lv, W. Yao, F. Xiao, Oxygen vacancies engineered CoMoO₄ nanosheet arrays as efficient bifunctional electrocatalysts for overall water splitting, J. Catal. 381 (2020) 44–52.
- [38] L. Zhang, T. Zhang, K. Dai, L. Zhao, Q. Wei, B. Zhang, X. Xiang, Ultrafine Co₃O₄ nanolayer-shelled CoWP nanowire array: a bifunctional electrocatalyst for overall water splitting, RSC Adv. 10 (2020) 29326–29335.
- [39] A. Badreldin, A.E. Abusrafa, A. Abdel-Wahab, Oxygen-deficient perovskites for oxygen evolution reaction in alkaline media: a review, Emerg. Mater. (2020) 1–24.
- [40] A. Badreldin, A. Abdel-Wahab, P.B. Balbuena, Local surface modulation activates metal oxide electrocatalyst for hydrogen evolution: synthesis, characterization, and DFT study of novel black ZnO, ACS Appl. Energy Mater. 3 (2020) 10590–11059.
- [41] A. Nezamzadeh-Ejehie, H. Zabihi-Mobarakeh, Heterogeneous photodecolorization of mixture of methylene blue and bromophenol blue using CuO-nanoclinoptilolite, J. Ind. Eng. Chem. 20 (2014) 1421–1431.
- [42] J. Tian, X. Hu, H. Yang, Y. Zhou, H. Cui, H. Liu, High yield production of reduced TiO₂ with enhanced photocatalytic activity, Appl. Surf. Sci. 360 (2016) 738–743.
- [43] M. Mondal, H. Dutta, S. Pradhan, Enhanced photocatalysis performance of mechano-synthesized V₂O₅-TiO₂ nanocomposite for wastewater treatment: Correlation of structure with photocatalytic performance, Mater. Chem. Phys. 248 (2020) 122947.
- [44] X. Cui, Z. Liu, G. Li, M. Zhang, Y. Song, J. Wang, Self-generating CeVO₄ as conductive channel within CeO₂/CeVO₄/V₂O₅ to induce Z-scheme-charge-transfer driven photocatalytic degradation coupled with hydrogen production, Int. J. Hydrog. Energy 44 (2019) 23921–23935.
- [45] B. Liu, D. Yin, F. Zhao, K.K. Khaing, T. Chen, C. Wu, L. Deng, L. Li, K. Huang, Y. Zhang, Construction of a novel Z-scheme heterojunction with molecular grafted carbon nitride nanosheets and V₂O₅ for highly efficient photocatalysis, J. Phys. Chem. C 123 (2019) 4193–4203.
- [46] M.A. Zeleke, D.-H. Kuo, Synthesis and application of V₂O₅-CeO₂ nanocomposite catalyst for enhanced degradation of methylene blue under visible light illumination, Chemosphere 235 (2019) 935–944.
- [47] P.K. Boruah, S. Szunerits, R. Boukherroub, M.R. Das, Magnetic Fe₃O₄@V₂O₅/rGO nanocomposite as a recyclable photocatalyst for dye molecules degradation under direct sunlight irradiation, Chemosphere 191 (2018) 503–513.
- [48] T.K. Le, M. Kang, S.W. Kim, Relation of photoluminescence and sunlight photocatalytic activities of pure V₂O₅ nanohollows and V₂O₅/RGO nanocomposites, Mater. Sci. Semicond. Process. 100 (2019) 159–166.
- [49] X. Liu, Z. Xing, H. Zhang, W. Wang, Y. Zhang, Z. Li, W. Zhou, Fabrication of 3 D mesoporous black TiO₂/MoS₂/TiO₂ nanosheets for visible-light-driven photocatalysis, ChemSusChem 9 (2016) 1118–1124.
- [50] H. Tan, Z. Zhao, M. Niu, C. Mao, D. Cao, D. Cheng, Z. Sun, A facile and versatile method for preparation of colored TiO₂ with enhanced solar-driven photocatalytic activity, Nanoscale 6 (2014) 10216–10223.
- [51] B. Ingham, M. Toney, X-ray diffraction for characterizing metallic films, Metallic Films for Electronic, Optical and Magnetic Applications, Elsevier, 2014, pp. 3–38.
- [52] Y.T. Prabhu, K.V. Rao, V.S.S. Kumar, B.S. Kumari, X-ray analysis by Williamson-Hall and size-strain plot methods of ZnO nanoparticles with fuel variation, World J. Nano Sci. Eng. 04 (2014) 21–28.
- [53] J.P. Perdew, K. Burke, M. Ernzerhof, Generalized gradient approximation made simple, Phys. Rev. Lett. 77 (1996) 3865–3868.
- [54] M. Ernzerhof, G.E. Scuseria, Assessment of the Perdew–Burke–Ernzerhof exchange–correlation functional, J. Chem. Phys. 110 (1999) 5029–5036.
- [55] G. Kresse, J. Furthmüller, Efficient iterative schemes for ab initio total-energy calculations using a plane-wave basis set, Phys. Rev. B 54 (1996) 11169–11186.
- [56] G. Kresse, D. Joubert, From ultrasoft pseudopotentials to the projector augmented-wave method, Phys. Rev. B 59 (1999) 1758–1775.
- [57] B. Himmetoglu, A. Floris, S. De Gironcoli, M. Cococcioni, Hubbard-corrected DFT energy functionals: the LDA+U description of correlated systems, Int. J. Quantum Chem. 114 (2014) 14–49.
- [58] M. Methfessel, A. Paxton, High-precision sampling for Brillouin-zone integration in metals, Phys. Rev. B 40 (1989) 3616–3621.
- [59] H.J. Monkhorst, J.D. Pack, Special points for Brillouin-zone integrations, Phys. Rev. B 13 (1976) 5188–5192.
- [60] Y. Li, Q. Du, T. Liu, X. Peng, J. Wang, J. Sun, Y. Wang, S. Wu, Z. Wang, Y. Xia, Comparative study of methylene blue dye adsorption onto activated carbon, graphene oxide, and carbon nanotubes, Chem. Eng. Res. Des. 91 (2013) 361–368.
- [61] B. Choudhury, S. Bayan, A. Choudhury, P. Chakraborty, Narrowing of band gap and effective charge carrier separation in oxygen deficient TiO₂ nanotubes with improved visible light photocatalytic activity, J. Colloid Interface Sci. 465 (2016) 1–10.
- [62] M.H. Farooq, I. Aslam, H.S. Anam, M. Tanveer, Z. Ali, U. Ghani, R. Boddula, Improved photocatalytic performance of reduced zinc oxide (ZnO) novel morphology of astray like microstructure under solar light irradiation, Mater. Sci. Energy Technol. 2 (2019) 181–186.
- [63] S. Senobari, A. Nezamzadeh-Ejehie, A comprehensive study on the photocatalytic activity of coupled copper oxide-cadmium sulfide nanoparticles, Spectrochim. Acta Part A Mol. Biomol. Spectrosc. 196 (2018) 334–343.
- [64] L. Ye, D. Wu, K.H. Chu, B. Wang, H. Xie, H.Y. Yip, P.K. Wong, Phosphorylation of g-C₃N₄ for enhanced photocatalytic CO₂ reduction, Chem. Eng. J. 304 (2016) 376–383.
- [65] F. Liang, Y. Zhu, Enhancement of mineralization ability for phenol via synergistic effect of photoelectrocatalysis of g-C₃N₄ film, Appl. Catal. B Environ. 180 (2016) 324–329.
- [66] Z. Amani-Beni, A. Nezamzadeh-Ejehie, A novel non-enzymatic glucose sensor based on the modification of carbon paste electrode with CuO nanoflower: designing the experiments by response surface methodology (RSM), J. Colloid Interface Sci. 504 (2017) 186–196.

- [67] A. Nezamzadeh-Ejhi, S. Hushmandrad, Solar photodecolorization of methylene blue by CuO/X zeolite as a heterogeneous catalyst, *Appl. Catal. A Gen.* 388 (2010) 149–159.
- [68] A. Nezamzadeh-Ejhi, M. Karimi-Shamsabadi, Comparison of photocatalytic efficiency of supported CuO onto micro and nano particles of zeolite X in photodecolorization of Methylene blue and Methyl orange aqueous mixture, *Appl. Catal. A Gen.* 47 (2014) 83–92.
- [69] M. Karimi-Shamsabadi, A. Nezamzadeh-Ejhi, Comparative study on the increased photoactivity of coupled and supported manganese-silver oxides onto a natural zeolite nano-particles, *J. Mol. Catal. A Chem.* 418 (2016) 103–114.
- [70] S.K. Jayaraj, V. Sadishkumar, T. Arun, P. Thangadurai, Enhanced photocatalytic activity of V_2O_5 nanorods for the photodegradation of organic dyes: a detailed understanding of the mechanism and their antibacterial activity, *Mater. Sci. Semicond. Process.* 85 (2018) 122–133.
- [71] Y. Lv, W. Yao, X. Ma, C. Pan, R. Zong, Y. Zhu, The surface oxygen vacancy induced visible activity and enhanced UV activity of a ZnO_{1-x} photocatalyst, *Catal. Sci. Technol.* 3 (2013) 3136–3146.
- [72] N. Omrani, A. Nezamzadeh-Ejhi, Focus on scavengers' effects and GC-MASS analysis of photodegradation intermediates of sulfasalazine by Cu_2O/CdS nanocomposite, *Sep. Purif. Technol.* 235 (2020) 116228.
- [73] N. Raeisi-Kheirabadi, A. Nezamzadeh-Ejhi, A Z-scheme $g-C_3N_4/Ag_3PO_4$ nanocomposite: Its photocatalytic activity and capability for water splitting, *Int. J. Hydrog. Energy* 45 (2020) 33381–33395.
- [74] C. Wang, D. Wu, P. Wang, Y. Ao, J. Hou, J. Qian, Effect of oxygen vacancy on enhanced photocatalytic activity of reduced ZnO nanorod arrays, *Appl. Surf. Sci.* 325 (2015) 112–116.
- [75] I. Singh, B. Birajdar, Synthesis, characterization and photocatalytic activity of mesoporous Na-doped TiO_2 nano-powder prepared via a solvent-controlled non-aqueous sol-gel route, *RSC Adv.* 7 (2017) 54053–54062.
- [76] M.H. Elsayed, T.M. Elmorsi, A.M. Abuelela, A.E. Hassan, A.Z. Alhakemy, M.F. Bakr, H.-H. Chou, Direct sunlight-active Na-doped ZnO photocatalyst for the mineralization of organic pollutants at different pH mediums, *J. Taiwan Inst. Chem. Eng.* 115 (2020) 187–197.
- [77] S. Gates-Rector, T. Blanton, The powder diffraction file: a quality materials characterization database, *Powder Diffraction* 34 (2019) 352–360.
- [78] B.N. Reddy, B.M. Reddy, M. Subrahmanyam, Dispersion and 3-picoline ammoxidation investigation of $V_2O_5/\alpha-Al_2O_3$ catalysts, *J. Chem. Soc. Faraday Trans.* 87 (1991) 1649–1655.
- [79] H. Nakao, K. Ohwada, N. Takesue, Y. Fujii, M. Isobe, Y. Ueda, H. Sawa, H. Kawada, Y. Murakami, W. David, Lattice dimerization and strain in inorganic spin-Peierls compound NaV_2O_5 , *Phys. B Condens. Matter* 241 (1997) 534–536.
- [80] T. Tamiji, A. Nezamzadeh-Ejhi, Electrocatalytic behavior of AgBr NPs as modifier of carbon past electrode in the presence of methanol and ethanol in aqueous solution: a kinetic study, *J. Taiwan Inst. Chem. Eng.* 104 (2019) 130–138.
- [81] K.Y. Jung, S.B. Park, S.-K. Ihm, Linear relationship between the crystallite size and the photoactivity of non-porous titania ranging from nanometer to micrometer size, *Appl. Catal. A Gen.* 224 (2002) 229–237.
- [82] E. Hryha, E. Rutqvist, L. Nyborg, Stoichiometric vanadium oxides studied by XPS, *Surf. Interface Anal.* 44 (2012) 1022–1025.
- [83] J. Su, X. Zou, J.-S. Chen, Self-modification of titanium dioxide materials by Ti^{3+} and/or oxygen vacancies: new insights into defect chemistry of metal oxides, *RSC Adv.* 4 (2014) 13979–13988.
- [84] J. Yan, G. Wu, N. Guan, L. Li, Z. Li, X. Cao, Understanding the effect of surface/bulk defects on the photocatalytic activity of TiO_2 : anatase versus rutile, *Phys. Chem. Chem. Phys.* 15 (2013) 10978–10988.
- [85] P. Shvets, O. Dikaya, K. Maksimova, A. Goikhman, A review of Raman spectroscopy of vanadium oxides, *J. Raman Spectrosc.* 50 (2019) 1226–1244.
- [86] Y. Wang, J. Cai, M. Wu, J. Chen, W. Zhao, Y. Tian, T. Ding, J. Zhang, Z. Jiang, X. Li, Rational construction of oxygen vacancies onto tungsten trioxide to improve visible light photocatalytic water oxidation reaction, *Appl. Catal. B Environ.* 239 (2018) 398–407.
- [87] J. Dhanalakshmi, S. Iyyapushpam, S. Nishanthi, M. Malligavathy, D.P. Padiyan, Investigation of oxygen vacancies in Ce coupled TiO_2 nanocomposites by Raman and PL spectra, *Adv. Nat. Sci. Nanosci. Nanotechnol.* 8 (2017) 015015.
- [88] D. Chapron, F. Cordero, M.D. Fontana, Characterization of oxygen vacancies in $SrTiO_3$ by means of anelastic and Raman spectroscopy, *J. Appl. Phys.* 126 (2019) 154101.
- [89] M. Morey, A. Davidson, H. Eckert, G. Stucky, Pseudotetrahedral $O3/2V$ O centers immobilized on the walls of a mesoporous, cubic MCM-48 support: preparation, characterization, and reactivity toward water as investigated by ^{51}V NMR and UV-Vis spectroscopies, *Chem. Mater.* 8 (1996) 486–492.
- [90] A. Hassani, A.A. Akl, Effect of Se addition on optical and electrical properties of chalcogenide $CdSSe$ thin films, *Superlattices Microstruct.* 89 (2016) 153–169.
- [91] S. Jafari, A. Nezamzadeh-Ejhi, Supporting of coupled silver halides onto clinoptilolite nanoparticles as simple method for increasing their photocatalytic activity in heterogeneous photodegradation of mixture of 4-methoxy aniline and 4-chloro-3-nitro aniline, *J. Colloids Interface Sci.* 490 (2017) 478–487.
- [92] J.P. Perdew, M. Levy, Physical content of the exact Kohn-Sham orbital energies: band gaps and derivative discontinuities, *Phys. Rev. Lett.* 51 (1983) 1884–1887.
- [93] F.F. Abdi, L. Han, A.H. Smets, M. Zeman, B. Dam, R. Van De Krol, Efficient solar water splitting by enhanced charge separation in a bismuth vanadate-silicon tandem photoelectrode, *Nat. Commun.* 4 (2013) 1–7.